Metals **2014**, *4*, 196-234; doi:10.3390/met4020196

OPEN ACCESS

metals

ISSN 2075-4701

www.mdpi.com/journal/metals/

Review

Non-Equilibrium Solidification of Undercooled Metallic Melts

Dieter M. Herlach

Institut für Materialphysik im Weltraum, Deutsches Zentrum für Luft- und Raumfahrt, DLR, Köln 51147, Germany; E-Mail: dieter.herlach@dlr.de; Tel.: +49-2203-6012332; Fax: +49-2203-61768

Received: 15 May 2014; in revised form: 3 June 2014 / Accepted: 4 June 2014 / Published: 20 June 2014

Abstract: If a liquid is undercooled below its equilibrium melting temperature an excess Gibbs free energy is created. This gives access to solidification of metastable solids under non-equilibrium conditions. In the present work, techniques of containerless processing are applied. Electromagnetic and electrostatic levitation enable to freely suspend a liquid drop of a few millimeters in diameter. Heterogeneous nucleation on container walls is completely avoided leading to large undercoolings. The freely suspended drop is accessible for direct observation of rapid solidification under conditions far away from equilibrium by applying proper diagnostic means. Nucleation of metastable crystalline phases is monitored by X-ray diffraction using synchrotron radiation during non-equilibrium solidification. While nucleation preselects the crystallographic phase, subsequent crystal growth controls the microstructure evolution. Metastable microstructures are obtained from deeply undercooled melts as supersaturated solid solutions, disordered superlattice structures of intermetallics. Nucleation and crystal growth take place by heat and mass transport. Comparative experiments in reduced gravity allow for investigations on how forced convection can be used to alter the transport processes and design materials by using undercooling and convection as process parameters.

Keywords: undercooling; containerless solidification; metastable solids; dendrite growth; supersaturated alloys; disordered superlattices; grain refinement; forced convection; microgravity

---

1. Introduction

Metallic materials are prepared from the liquid state as their parent phase. The conditions under which the liquid solidifies determine the physical and chemical properties of the as-solidified material. In most cases, time and energy consuming post-solidification treatment of the material is mandatory to obtain the final product with its desired properties and design performance. Therefore, efforts are directed towards virtual material design with computer-assisted modelling. This can shorten the entire production chain—ranging from casting the shaped solid from the melt, to the final tuning of the product in order to save costs during the production process. The goal is to fabricate novel materials with improved properties for specific applications.

Computational material science, from the liquid state, requires detailed knowledge of the physical mechanisms involved in the solidification process. In particular, these are crystal nucleation and crystal growth. Both of these processes are driven by an undercooling of the liquid below its equilibrium melting temperature to develop conditions where a driving force for the formation of supercritical nuclei and the advancement of a solidification front are created. This gives access to non-equilibrium solidification pathways, which can form metastable solids, which may differ in their physical and chemical properties from their stable counterparts. Detailed modelling of solidification, far away from thermodynamic equilibrium, requires that every detail of the solidification process must be investigated.

In order to achieve the state of an undercooled melt, it is advantageous to remove heterogeneous nucleation sites, which, otherwise, limit the undercoolability. The most efficient way to realize such conditions is the containerless processing of melts [1]. In such a process, the most dominant heterogeneous nucleation process, involving interaction with container walls, is completely avoided. Nowadays, electromagnetic [2] and electrostatic levitation techniques [3,4] have been developed for containerless undercooling and solidification of molten metals and alloys. A freely suspended drop gives the extra benefit of being able to directly observe the solidification process by combining the levitation technique with proper diagnostic means [5,6]. Short range ordering in undercooled metallic melts, as precursor of crystal nucleation, has been investigated by using neutron diffraction [7] and diffraction of synchrotron radiation [8] on containerless undercooled melts [9]. Additionally, primary phase selection processes for rapid solidification of metastable phases has been observed *in situ* by energy dispersive X-ray diffraction using synchrotron radiation of high intensity [10]. Rapid growth of dendrites is observed on levitation-undercooled melts by using video camera techniques, characterized by high spatial and temporal resolution [11].

During crystallization of a melt, the heat of crystallization is released, which leads to a temperature rise during the initial solidification. In the case of containerless processing, heat is transferred by heat radiation under Ultra-High-Vacuum conditions (e.g., in electrostatic levitation) and, additionally, by heat conduction in an environmental gas if the sample is processed in an inert noble gas atmosphere (e.g., in electromagnetic levitation). If the sample is undercooled prior to solidification, the initial crystallization process is very rapid. As a consequence, the production of heat, due to the rapid release of the heat of crystallization, occurs much more rapidly than the transfer of the heat of the sample to the environment. Therefore, the undercooled melt serves as a heat sink. This leads to a temperature rise during the initial crystallization of the sample known as recalescence. The non-equilibrium process of rapid solidification is accessible to direct analysis by investigating the recalescence profile.

Both nucleation and subsequent crystal growth are governed by heat and mass transport. Thus, any transport process stimulated externally by natural convection and/or forced convection due to stirring effects of alternating electromagnetic fields in electromagnetic levitation experiments may cause a serious influence on the solidification process. To understand this effect, and to develop a quantitative description of crystallization in the presence of forced convection, comparative experiments on Earth and in reduced gravity are of great help. Under the special conditions of reduced gravity, for instance, in Space, the forces needed to compensate disturbing accelerations are about three orders of magnitude smaller than the force needed to compensate the gravitational force for levitation experiments on Earth. In a cooperative effort by the European Space Agency (ESA) and the German Space Center—Space Management (DLR), a facility for Electro-Magnetic Levitation (EML) is under constructions for use in reduced gravity. Launch of this facility to the *Columbus* European module of the International Space Station (ISS) is scheduled for summer 2014. International research teams prepared experiments using the EML multiuser facility for investigations on undercooled metallic melts in space [12].

The present article aims to give an overview on the current state of research on undercooled melts and their non-equilibrium solidification.

2. Crystallization

2.1. Crystal Nucleation

Crystal nucleation is the first step in crystallization of undercooled melts. It selects the crystallographic phase, may it be stable or metastable. Within nucleation theory, one distinguishes between homogeneous and heterogeneous nucleation. Homogeneous nucleation is an intrinsic process that depends exclusively on materials properties. In contrast, heterogeneous nucleation is an extrinsic process in which, besides the undercooled liquid and the crystal nucleus, a third partner is involved. This can be a foreign phase, surface oxides, and/or container walls. In particular, container walls are involved in crystal nucleation of metallic melts because they are contained in a crucible. They are acting as catalysts of nucleation, decreasing the activation energy to form nuclei of supercritical size. If heterogeneous nucleation is avoided, the onset of homogeneous nucleation will initiate crystallization. The formation of a homogeneous nucleus requires the maximum activation energy and, therefore, gives the limit of maximum undercooling of a melt.

2.1.1. Homogeneous Nucleation

The electrostatic levitator is very suitable to study nucleation undercooling with special emphasis to homogeneous nucleation. To observe homogeneous nucleation, very large undercoolings have to be realized, as the onset of homogeneous nucleation gives the physical limit for maximum undercoolability of a melt. To realize such conditions, heterogeneous nucleation has to be eliminated. Electrostatic levitation under Ultra-High-Vacuum is ideally suited for such experimental studies since heterogeneous nucleation on container walls is completely avoided and heterogeneous nucleation on surface motes is reduced, or even eliminated, due to self-cleaning of the surface by evaporation at elevated temperature.

Nucleation undercooling studies on pure Zr are presented to demonstrate how physically different nucleation processes are experimentally investigated. Figure 1 shows a temperature-time-profile measured on pure Zr sample in the electrostatic levitator (*cf.* inset). The solid sample is heated up to its melting temperature, T_L. In the case of a pure metal, such as Zr, the sample melts congruently at T_L. The small step in the melting plateau is due to the change in spectral emissivity when the solid transforms to a liquid. After complete melting, the liquid sample is heated to a temperature well above T_L before cooling. During subsequent cooling, the liquid sample undercools well below T_L. When spontaneous nucleation sets in at an undercooling, $\Delta T = T_L - T_n$ (T_n: nucleation temperature), the nucleated crystal grows rapidly due to a large thermodynamic driving force generated at such deep undercoolings. The rapid release of the heat of crystallization leads to a steep rise of temperature during recalescence. From such temperature-time profiles, ΔT is easily inferred since T_n is well defined by the onset of recalescence. After the entire sample has solidified, the next heating and cooling cycle is started.

Figure 1. Temperature-time profile measured on a zirconium drop levitated in an electrostatic levitator. The sample melts at T_L = 2128 K. During undercooling nucleation sets in at T_N = 1757 K. Subsequently, rapid crystal growth of β-Zr solid phase (bcc) leads to a steep rise of temperature during recalescence. The second recalescence event at 980 K is attributed to a transformation of solid β-Zr to solid α-Zr phase (hcp). The inset shows the determination of the undercooling from the measured temperature-time profile.

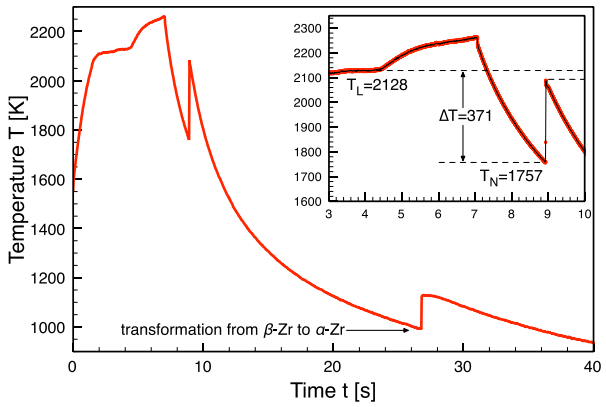

Usually, the solidification of an undercooled metallic melt is a two-stage process. During recalescence a fraction of the sample, f_R, solidifies during recalescence under a non-equilibrium condition. The remaining melt, $f_{pr} = 1 - f_R$, solidifies under near-equilibrium conditions during post-recalescence period. f_R increases with the degree of undercooling and becomes unified, $f_R = 1$ if $\Delta T = \Delta T_{\mathrm{hyp}}$. The hypercooling limit, ΔT_{hyp}, is reached if the heat of fusion ΔH_f is just sufficient to heat the sample with its specific heat C_p up to T_L. In the case of quasiadiabatic conditions, *i.e.*, if the amount of heat transferred to the environment is negligible compared to the heat produced during recalescence, the hypercooling limit is given by $\Delta T_{hyp} = \Delta H_f/C_p$. In the case of pure Zr, the hypercooling limit is estimated as ΔT_{hyp} = 359 K with ΔH_f = 14652 J/mol and C_p = 40.8 J·mol/K. With increasing undercooling, $\Delta T' > \Delta T_{hyp}$, the post-recalescence plateau vanishes and T_L will not be reached during recalescence. In this experiment, an undercooling of ΔT = 371 K is measured, which is larger than ΔT_{hyp}.

Figure 2 shows the distribution functions of undercoolings measured in the electromagnetic levitator (left) and the electrostatic levitator (right). The experimental results are analysed within a statistical model developed by Skripov [13]. According to nucleation theory [14], the activation energy, ΔG^*, for the formation of a nucleus of critical size is given by:

$$\Delta G^* = \frac{16\pi}{3} \cdot \frac{\sigma^3}{\Delta G_V^2} \cdot f(\vartheta) \tag{1}$$

with σ the solid-liquid interfacial energy, $\Delta G_V = G_L - G_S$, the difference of Gibbs free energy per unit volume of liquid, G_L and solid G_S phase, and $f(\vartheta)$ the catalytic potency factor for heterogeneous nucleation with ϑ the wetting angle. In the case of homogeneous nucleation, $f(\vartheta) = 1$.

For pure metals, the driving force for nucleation, ΔG_V, is approximated by $\Delta G_V = \Delta S_f \cdot \Delta T \cdot V_m^{-1}$ with $\Delta S_f = \Delta H_f / T_m$ and ΔH_f the enthalpy of fusion and V_m the molar volume [15]. The solid-liquid interfacial energy σ is given by the negentropic model [16] as:

$$\sigma = \alpha \cdot \frac{\Delta S_f \cdot T}{(N_A V_m)^{1/3}} \tag{2}$$

with N_A Avogadro's number and the dimensionless interfacial energy $\alpha = 0.7$ for bcc structured solid β-Zr that primarily nucleates in the undercooled melt. The steady state nucleation rate, I_{ss}, is computed by:

$$I_{ss} = K_V \cdot \exp\left(-\frac{\Delta G^*}{k_B T}\right) = K_V \cdot \exp\left(-\frac{CT^2}{\Delta T^2}\right) \text{with } K_V = \frac{k_B T N_o}{3 a_o \eta(T)}; C = \frac{16\pi \Delta S_f \alpha^3 f(\vartheta)}{3 k_B N_A} \tag{3}$$

where $\eta(T)$ denotes the temperature dependent viscosity, a_o a typical interatomic spacing, k_B Boltzmann's constant, and N_0 the number of potential nucleation sites. For homogeneous nucleation, K_V in Equation (3) is of the order of $K_V \approx 10^{+39}$ $\mathrm{m^{-3} \cdot s^{-1}}$ [17] or even $K_V \approx 10^{+42}$ $\mathrm{m^{-3} \cdot s^{-1}}$ [18] because each atom in the melt can act as a potential nucleation site, $N_0 = N_A/V_m$. The prefactor is estimated from the product of Avogadro's number and the impingement frequency that is of the order of the Debye frequency, 10^{-13} Hz. In case of heterogeneous nucleation, only atoms at the catalysing substrate can act as a nucleation site. Therefore, N_0 and, hence, K_V, are drastically reduced in case of heterogeneous nucleation, as compared with homogeneous nucleation.

Nucleation is a stochastic process of rare and independent events. Therefore, the Poisson distribution is applied to determine K_V and C of Equation (3) from the distribution function of the measured undercoolings. Under non-isothermal conditions (cooling rate $T \neq 0$), the probability for one nucleation event in a sample of volume V is given by:

$$\omega(1, T + \delta T) = \delta T \frac{V I_{ss}(T)}{\left|\dot{T}\right|} \div \exp\left[-\int_{T_m}^{T} \frac{V I_{ss}(T)}{\dot{T}} \mathrm{d}T\right] \tag{4}$$

From these Equations (3) and (4) the cumulative distribution function $F(T)$ is determined:

$$F(T) = 1 - \exp\left[-\frac{V}{\dot{T}} \int_{T_m}^{T} K_V \cdot \exp\left(\frac{CT^2}{\Delta T^2}\right) \mathrm{d}T\right] \tag{5}$$

Large undercoolings were achieved by levitation techniques. In the case of electrostatic levitation, the undercoolings are about 50 K larger than in case of electromagnetic levitation. From the analysis

within the Skripov model, the activation energy ΔG^* and the prefactor in the nucleation rate, K_V, are inferred. Both quantities are characterizing the nucleation process. In the case of electromagnetic levitation, the analysis suggests heterogeneous nucleation to be dominant. The investigations by using the electrostatic levitator hint to maximum undercoolings as limited by the onset of homogeneous nucleation. Assuming homogeneous nucleation, the solid-liquid interfacial energy is estimated within classical nucleation theory, which is otherwise not accessible for experimental determination.

Equation (5), in combination with the results of the statistical analysis, yields the product $\alpha \cdot f(\vartheta)^{1/3} = 0.61$ for Zr from the undercooling experiments in the ESL. In the literature, a great variety of dimensionless solid-liquid interfacial energies are reported from modelling work. From the present investigations, the different approaches of solid-liquid interface modelling are evaluated by comparing the modelling results with findings inferred from maximum undercooling of Zr in electrostatic levitation experiments. Since the prefactor, K_V, is comparable in the order of magnitude to the value given by Turnbull for homogeneous nucleation, $f(\vartheta) \approx 1$ is assumed. This leads to a lower limit of the dimensionless interfacial energy $\alpha \geq 0.61$. The comparison with the modelling results shows that the negentropic model, with $\alpha = 0.70$ [16], gives the best agreement with the present experiment. Density-functional theory yields $\alpha = 0.46$ and $\alpha = 0.48$ [19] and molecular dynamics simulations yield $\alpha = 0.29$, $\alpha = 0.32$, and $\alpha = 0.36$, respectively [20], depending on the potentials used for the simulations. All these values underestimate the solid-liquid interfacial energy inferred from the experiments. Only the negentropic model by Spaepen is in agreement with the experiments. More details are given in [21].

Figure 2. Probability distribution functions of undercoolings measured in approximately 100 cycles on pure Zr in the electromagnetic (red bars) and the electrostatic levitator (green bars) [21]. The solid lines give the functions, as computed according to a statistical analysis of nucleation within the Skripov model.

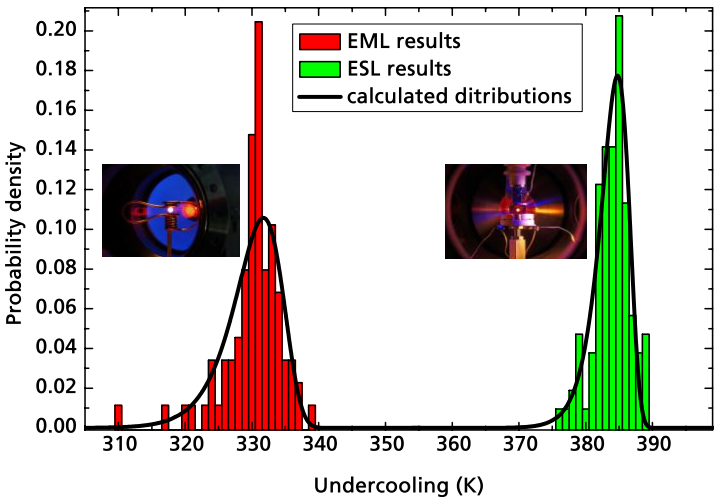

2.1.2. Catalysis of Metastable Phase Nucleation by External Triggering

A freely suspended liquid drop offers the unique possibility to externally stimulate heterogeneous nucleation by touching the undercooled drop with a nucleation-triggering needle. The principle of such an experiment is shown in Figure 3, on the left hand side. The crystallization needle is used to trigger, externally, solidification at a preselected undercooling and a well-defined position at the surface of the sample. In such a way, the crystallization kinetics is investigated as a function of undercooling [22]. Figure 3 illustrates triggered nucleation of a metastable bcc phase of Fe-24 at%Ni alloy. A trigger needle made of a $Fe_{95}Mo_5$ alloy is used since this alloy forms a stable bcc structure in the temperature range of the present experiment. In the Figure 3, right hand side the left peak represents a recalescence event, as observed following spontaneous nucleation at 1472 K (ΔT = 278 K). An increase of temperature up to 1751 K is found in good agreement with the equilibrium liquidus temperature of this alloy. Apparently, spontaneous crystallization leads to the formation of the stable fcc phase, even at large undercoolings. The right peak was observed following solidification-triggering with the Fe-Mo tip at a temperature of 1556 K (ΔT = 194 K). Obviously, the increase of temperature during recalescence ends at a temperature well below the equilibrium liquidus line, which points to a metastable bcc solidification product. Immediately following the recalescence peak, a weak hump is found in the cooling trace, which is due to a solid-state transformation of primarily formed metastable bcc phase into stable fcc phase. This hump is missing in the temperature-time profile for the spontaneous nucleation. This confirms that during spontaneous crystallization the fcc phase is nucleated, whereas triggered solidification leads to nucleation of a metastable bcc phase, which, however, transforms into the stable fcc phase during cooling of the sample to ambient temperature [23]. This means that the analysis of the as-solidified alloy does not allow for unambiguous determination of phase selection processes during rapid crystallization of deeply undercooled metallic alloys.

Figure 3. (**Left**) Principle of nucleation triggering of a metastable bcc phase in $Fe_{76}Ni_{24}$ alloy by using a nucleation trigger made of $Fe_{95}Mo_5$ bcc phase. (**Right**) Two temperature-time profiles obtained during solidification of undercooled $Fe_{76}Ni_{24}$ alloy. Spontaneous crystallization of stable fcc phase (γ, blue line), and solidification of a metastable bcc phase upon triggering with the $Fe_{95}Mo_5$ nucleation trigger (green line).

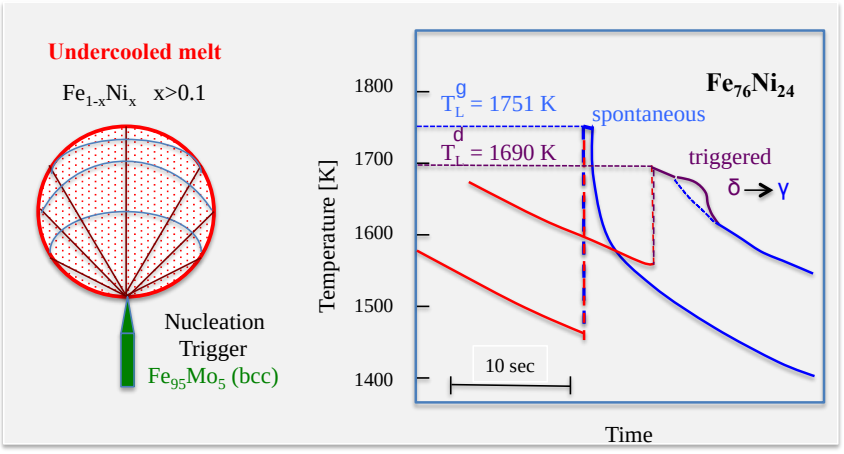

The cooling rates of the order of 10–100 K/s in the above-described undercooling experiments on Fe-Ni alloys are not sufficient to conserve the primary solidified metastable bcc phase during cooling to ambient temperatures. If the cooling rate is increased up to 10^5–10^6 K/s, the solid-state transformation of primary formed bcc phase into the stable fcc phase can be, however, partly avoided. This has been demonstrated in the early drop-tube experiments by Cech [24,25], and, later on, by atomization experiments [26]. Meanwhile, an electromagnetic levitation chamber is used to combine it with external diagnostic means, e.g., neutron scattering and X-ray scattering by synchrotron radiation [5]. The primary crystallization of a metastable bcc phase in Ni-V alloys at large undercoolings was directly evidenced by *in situ* energy dispersive X-ray diffraction on levitation processed undercooled melt, using high intensity synchrotron radiation at the European Synchrotron Radiation Facility [6]. This becomes possible as a full diffraction spectrum is recorded in a very short time interval of less than 0.5 s.

2.1.3. Experimental Determination of Metastable Phase Diagrams

By systematic investigations, as a function of concentration and undercooling using this diagnostic means, complete metastable phase diagrams have been experimentally constructed as, well-shown, in Figure 4, for the Ni-V alloy system [10]. This alloy crystallizes in three different phases, depending on the concentration. With increasing vanadium fraction, the equilibrium solidification changes from primary α-Ni (fcc) to an intermetallic phase σ’ (tetragonal), and, finally, to β-V (bcc). Upon undercooling, the three phases compete. The metastable bcc β-V phase has been primarily formed beyond a critical undercooling within the ranges of the stable α-Ni and σ’ phases. Diffraction pattern 1, taken from a melt undercooled by 50 K below the liquidus temperature T_l (σ’), shows diffuse maxima characteristic of a liquid. Diffraction pattern 2 reveals that, at ΔT = 60 K, a part of the undercooled melt crystallized into the metastable bcc phase during the weak recalescence. The bcc phase grows continuously upon further cooling (diffraction pattern 3) until the second reaction sets in at ΔT = 120 K, where reflections of the equilibrium σ’ phase emerge. At the same time, the bcc phase completely disappears, either by remelting or via a liquid–solid reaction. For lower vanadium concentrations, only primary nucleation of the equilibrium fcc phase was observed, even though, for some compositions, the undercooling was well below T_{lm} (β)—the metastable extension of the liquidus temperature of the β-V phase. However, after several seconds, the bcc phase was formed during the second crystallization event. The nucleation and growth of the metastable bcc phase did not influence the intensity of the fcc phase reflections, thus, one may conclude it grows from the undercooled melt independently. Again, the metastable phase decomposes after crystallization of the remaining liquid into a mixture of the equilibrium phases, σ’ and fcc. Although the observed formation of the metastable bcc phase is thermodynamically viable, its nucleation before the σ’ phase, which, in general, possesses a lower solid–liquid interfacial energy, can only be explained by the catalytic effect of the oxides, triggering the heterogeneous nucleation of the bcc phase at the droplet surface [6]. These investigations unambiguously demonstrate that *in situ* observations of phase selection processes are needed to develop a complete understanding of the formation of different crystallographic phases, stable or metastable, during non-equilibrium solidification of deeply undercooled melts while, *post mortem* analyses of as-solidified samples are not sufficient to explore the entire crystallization

history. Primarily formed crystalline phases can transform to the stable crystalline phase during the post-recalescence period by remelting processes or even during cooling by solid-solid phase transformations. Quenching the levitated drop immediately after recalescence allows to freezing in the primarily crystallized metastable phase, as reported from similar experimental investigations of phase selection of steel alloys and refractory metals [27].

Figure 4. (**a**) nucleation map of Ni-V system after [10]. The symbols mark the primarily solidified phases as a function of composition and nucleation temperature. Metastable extensions of the equilibrium liquidus lines are shown by dotted lines. (**b**) Temperature–time profile and (**c**) corresponding X-ray diffraction patterns recorded during solidification of a levitated $Ni_{41}V_{59}$ alloy. Numbers 1–4 mark the time at which the patterns are recorded. Related liquidus temperatures of the stable σ' and the metastable bcc and stable fcc phases are shown. A part of the undercooled melt (pattern 1) primarily crystallizes into the metastable bcc phase (pattern 2 and 3) followed up by the crystallization of the intermetallic σ' phase (pattern 4), taken from [6].

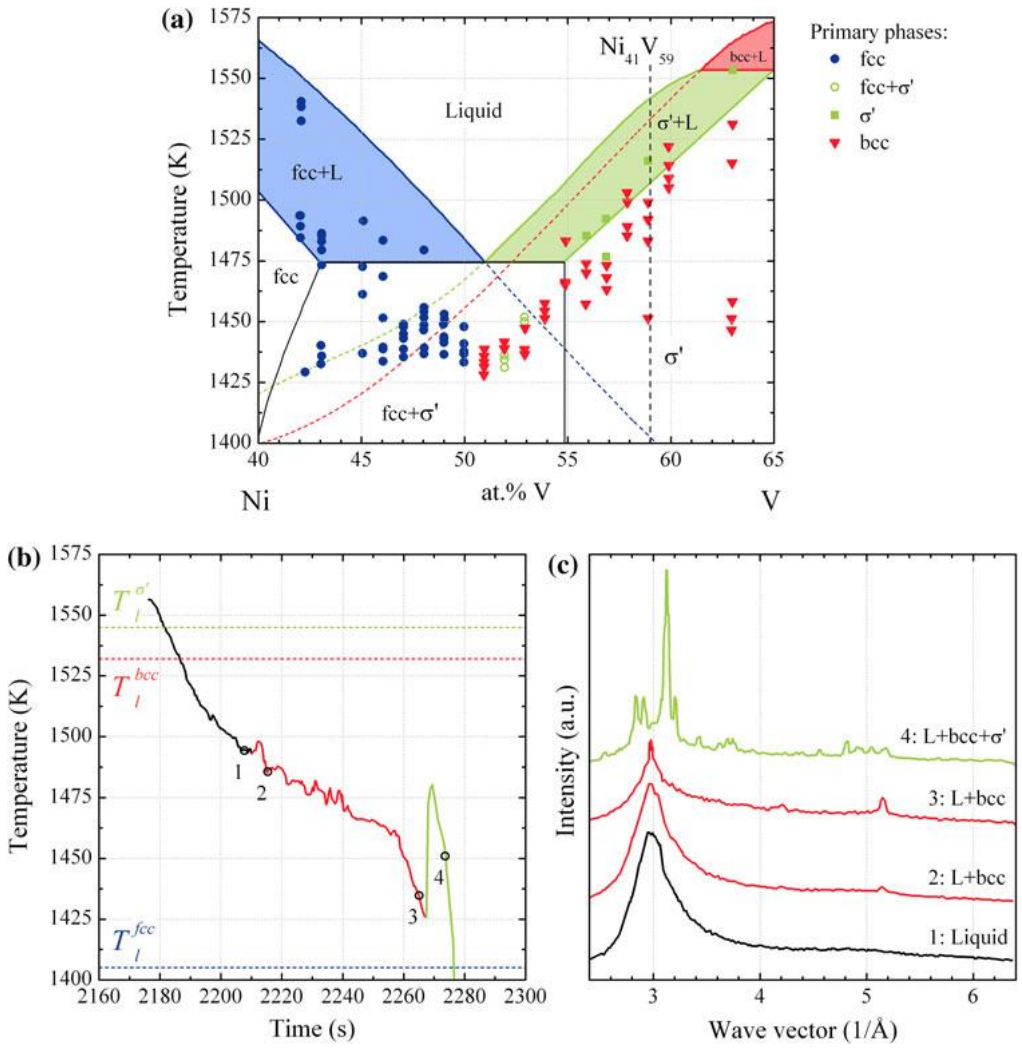

Nucleation preselects the crystallographic phase stable or metastable in undercooled melts. Subsequent crystal growth controls the evolution of metastable microstructures. The latter one will be discussed in the next section.

2.2. Crystal Growth

Crystal growth in undercooled melts leads to a heating up the solid-liquid interface due to the release of the heat of crystallization. As a consequence, a negative temperature gradient will be established in front of the interface since the undercooled melt acts as a heat sink. This will destabilize the initially planar interface. In alloys, a concentration gradient will be built up in addition. Due to limited solubility of the solute in the solid phase, compared to the liquid phase, solute will pile up in front of the interface. The resulting concentration gradient will reinforce, in addition to the negative temperature gradient, the instability of the solidification front. Eventually, the morphological destabilization of an initially planar interface will lead to dendrite growth. Dendrites consist of the main stem and side-branches, which grow into the melt.

2.2.1. Sharp Interface Theory of Dendrite Growth

An extended model of sharp interface theory is applied to describe the growth dynamics of dendrites as a function of undercooling [28,29]. Accordingly, the total undercooling measured in the experiment is expressed as the sum of various contributions:

$$\Delta T = \Delta T_T + \Delta T_R + \Delta T_N + \Delta T_K + \Delta T_C \quad (6)$$

with ΔT_T the thermal undercooling, ΔT_R the curvature undercooling, ΔT_N the undercooling due to the shift of the equilibrium slope of the liquidus m_E to its non-equilibrium value m_V, ΔT_K the kinetic undercooling, and ΔT_C the constitutional undercooling, respectively. The thermal undercooling $\Delta T_T = T_i - T_\infty$ with T_i the temperature at the tip of the dendrite and T_∞ the temperature of the undercooled melt far from the interface is expressed by:

$$\Delta T_T = \Delta T_{\mathrm{hyp}}\, Iv(Pe_T) \quad (7)$$

$Iv(Pe_T) = Pe_T \exp(Pe_T)\, E_1$ is the Ivantsov function for heat diffusion with $Pe_T = (VR)/2a$ the thermal Peclet number, V the velocity of the tip of the dendrite, R the radius of curvature at the tip of the dendrite, and a the thermal diffusivity. E_1 denotes the first exponential integral function. Due to the strong curvature of the dendrite tip, a reduction of the melting temperature, due to the Gibbs Thomson effect, has to be taken into account by the curvature undercooling $\Delta T_R = T_L - T_i$ with T_L the liquidus temperature and T_i the temperature at the tip:

$$\Delta T_R = 2\,\Gamma\,(1 - 15\varepsilon_s \cos 4\theta)/R \quad (8)$$

where $\Gamma = \sigma/\Delta S_f$ (σ: interface energy, ΔS_f the entropy of fusion) is the capillary constant (Gibbs-Thomson parameter), ε_s is the parameter of anisotropy of the interface energy, and θ is the angle between the normal to the interface and the direction of growth along the growth-axis. ΔT_N takes into account the change of liquidus line, due to deviations from equilibrium at large dendrite growth velocities, and is expressed by:

$$\Delta T_N = (m_E - m(V))\, C_o \quad (9)$$

m_E is the slope of liquidus line of the equilibrium phase diagram and $m(V)$ is the slope of the liquidus line in the kinetic phase diagram at nominal composition C_o.

The kinetic undercooling ΔT_K is given by:

$$\Delta T_K = V/\mu;\ \mu = \mu_o(1 - \varepsilon_K \cos 4\theta) \tag{10}$$

where μ is the kinetic growth coefficient for growth of the dendrite tip, ε_K is the parameter of anisotropy for the growth kinetics [30] and is determined by atomic simulations [31]. The kinetic undercooling is controlled by the atomic attachment kinetics at the solid-liquid interface that can differ essentially for specific atomic bonding conditions and structural peculiarities. Investigations of the growth kinetics in an undercooled melt of the intermetallic compound $Cu_{50}Zr_{50}$ that melts congruently, and is a glass forming alloy with highly reduced glass temperature, gives evidence of dendrite growth to be controlled by atomic diffusion in the temperature range above the glass temperature [32]. In non-congruently melting alloys, chemical mass transport by segregation has to be considered. The constitutional undercooling in alloys with solidification interval is given by:

$$\Delta T_C = m_V C_o (k(V) - 1)\, Iv(Pe_C)/[1 - (1 - k(V))\, Iv(Pe_C)] \tag{11}$$

$Pe_C = (VR)/2D$ is the Péclet number of mass diffusion with D the diffusion coefficient, $Iv(Pe_C) = Pe_C\ exp(Pe_C)\ E_1$ the Ivantsov function for mass diffusion, $k(V)$ the velocity dependent partition coefficient. Under the conditions of rapid solidification, for the range of growth velocity $V < V_D$ (where V_D is the atomic diffusive speed in the bulk liquid), the liquidus slope is described by [33]:

$$\begin{aligned} m(V) &= \frac{m_E}{1 - k_E}\left\{1 - k(V) + \ln\left(\frac{k(V)}{k_E}\right) + \left(1 - k(V)\right)^2 \frac{V}{V_D}\right\}, \quad V < V_D \\ m(V) &= \frac{m_E \ln k_E}{k_E - 1}, \qquad\qquad V \geq V_D \end{aligned} \tag{12}$$

with k_E the partition coefficient of the equilibrium phase diagram. The solute partitioning as a function of growth velocity is described by the non-equilibrium partition coefficient $k(V)$, which becomes dependent on the growth velocity for the case of rapid solidification [34]:

$$\begin{aligned} k(V) &= \frac{\left(1 - V^2/V_D^2\right)\left[k_E + (1 - k_E)C_o\right] + V/V_{Di}}{1 - V^2/V_D^2 + V/V_{Di}}, V > V_D \\ k(V) &= 1, \qquad\qquad V \geq V_D \end{aligned} \tag{13}$$

with V_{Di} the interface diffusion velocity obtained by dividing the diffusion coefficient in the solid-liquid interface by the interatomic spacing. The diffusion coefficient in the interface is smaller compared with the bulk diffusion coefficient [35]. Equation (6) describes the relation of undercooling in terms of the Péclet numbers, *i.e.*, as a function of the product $V R$. For unique determination of the growth velocity V and tip radius R as a function of undercooling, ΔT one needs a second equation for the tip radius R, which comes from stability analysis:

$$R = \frac{\Gamma}{\sigma_o}\left[\frac{\Delta H_f}{C_p^l} Pe_T \xi_T(Pe_T) + \frac{2m(V)C_o(k(V) - 1}{1 - (1 - k(V))Iv(Pe_C)} Pe_C \xi_C(Pe_C)\right]^{-1} \tag{14}$$

ξ_T and ξ_C are the stability functions depending on the thermal and the chemical Péclet number. They are given by:

$$\xi_T(Pe_T) = \frac{1}{\left(1 + a_1 \varepsilon^{1/2} Pe_T\right)^2}, \qquad \xi_C(Pe_C) = \frac{1}{\left(1 + a_2 \varepsilon^{1/2} Pe_C\right)^2} \tag{15}$$

and are defined by the stiffness $\varepsilon = 15\varepsilon_C$ for a crystal with cubic symmetry and with the anisotropy ε_C of the interface energy. The parameters σ_o, a_1, and a_2 are obtained by fitting to experimental data, or from an asymptotic analysis as described in [36].

Since we are dealing with solidification of electromagnetically levitated drops, forced convection, induced by the strong alternating electromagnetic fields needed to levitate the drop, has to be taken into account. Accordingly, the thermal undercooling $\Delta T_T = T_i - T_\infty$ is expressed by [37]:

$$\Delta T_T = \Delta T_{hyp} Pe_T \exp\left(Pe_T + Pe_T^f\right) \cdot \int_1^\infty q^{-1} \exp\left[-qPe_T + (\ln q - q)Pe_T^f\right] \mathrm{d}q \tag{16}$$

where $\Delta T_{hyp} = \Delta H_f / C_p$ is the hypercooling temperature of solidification, defined as the ratio of the heat of fusion, ΔH_f and the heat capacity of the liquid C_p, $Pe_T^f = U_o R/(2a)$ is the flow thermal Péclet number, with U_o the velocity of the uniformly forced flow far from the dendrite tip. We estimate the fluid flow velocity from the energy balance between the electromagnetic field, the gravitational field, and the viscous dissipation:

$$U_o = \left[\frac{2}{\rho}\left(\rho g R_o + \frac{B_o^2\left(1 - \exp\left(2 R_o / \delta\right)\right)}{8\pi} + \frac{\rho\eta^2}{2\delta^2}\right)\right]^{1/2} \tag{17}$$

where g is the modulus of vector of the gravity acceleration, ρ is the mass density, η is the dynamic viscosity of the liquid phase, δ is the skin depth, R_o is the radius of the sample, and B_o is the time averaged value of the magnetic field inside the levitation coil. Using typical parameters of a metallic system and regarding the boundary conditions of electromagnetic levitation experiments, typical fluid flow velocities in liquid metallic drops are determined, ranging in the order of magnitude of several tenths of centimeters per second. This is in agreement with magnetohydrodynamic simulations and experimental observations [38].

In case of forced convection inside the melt, the stability parameter σ^* becomes dependent on the fluid flow velocity U_o. It is given by:

$$\sigma^* = \sigma_o \varepsilon_c^{7/4} \cdot \left[1 + \chi(\mathrm{Re}) \frac{U_o \Gamma}{a \Delta T_{hyp}}\right]^{-1} \tag{18}$$

where σ_o is a constant; $Re = U_o R/\eta$ is the Reynolds number. The function χ(Re) can be found in [39]. For computation of the stability parameter σ^* we choose the results of phase-field modelling [40] with $\sigma_o \varepsilon_c^{7/4}/\sigma^* = 1.675$ for the 3D upstream fluid flow imposed on the scale of a freely growing dendrite. Thus, from the two main Equations (6) and (14), the velocity V and the tip radius R of the dendrite can be calculated as a function of the initial undercooling ΔT.

To analyse further the influence of convection on solidification kinetics, we have used the "thin-interface" analysis of the phase-field model according to the work by Karma *et al.* [41], where the interface thickness is assumed to be small compared to the scale of the crystal, but not smaller than the microscopic capillary length. The phase-field and energy equations were taken from the model with the momentum and continuity equations of motion of the liquid phase as developed by Beckermann *et al.* [42]. Figure 5 illustrates the growth of an equiaxed dendrite, without (left) and with (right) flow. The green lines in Figure 5 represent the flow direction that is directed downwards. The simulation clearly shows how the growth kinetics is influenced by fluid flow. The branch of the dendrite growing opposite to the fluid stream (up-stream branch) develops much faster than the branch of the dendrite growing parallel with the fluid stream (down-stream branch) on the opposite side. Without any fluid flow, the equiaxed dendrite is symmetric.

Figure 5. Equiaxed dendrite within an undercooled liquid, without (**left**) and with (**right**) convection; fluid flow streams from top to bottom on the right picture; results from phase field modelling [37].

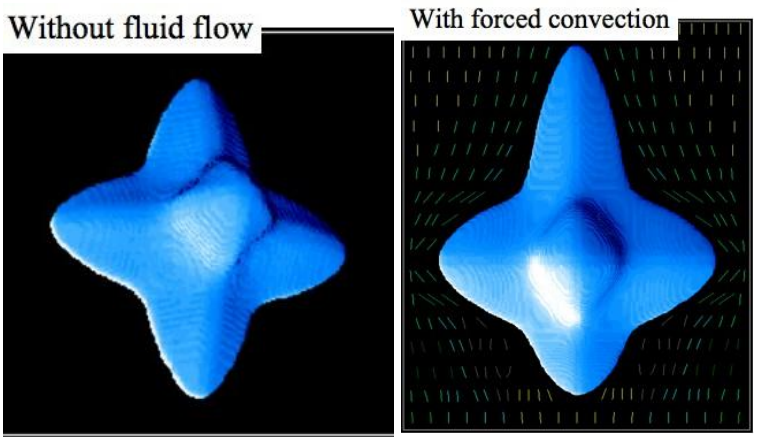

2.2.2. Influence of Forced Convection on Dendrite Growth Kinetics

$Al_{50}Ni_{50}$ was chosen for the investigations on growth kinetics under the conditions of forced convection on Earth and reduced convection in reduced gravity [43]. This alloy melts congruently and forms an intermetallic B2 β-phase under equilibrium conditions. Crystallization of ordered superlattice structures requires short-range atomic diffusion at the solid-liquid interface. This leads to sluggish growth dynamics, at least at small and intermediate undercoolings (V: 0.1–0.5 m/s) [44]. These growth velocities are directly comparable to the speed of fluid flow in levitated metallic melts due to the strong stirring effects of the alternating electromagnetic field [45]. Fluid flow motion inside the liquid drop changes the growth dynamics. This effect, however, will be reduced if the liquid drops are processed in a reduced gravity environment since electromagnetically induced convection and natural convection are much less pronounced. Figure 6 shows the results of measurements of dendrite growth velocity as a function of undercooling for $Al_{50}Ni_{50}$ alloy, both under terrestrial conditions (circles) and in reduced gravity (diamonds). All growth velocities measured in reduced gravity are significantly smaller than those determined under terrestrial conditions. At growth velocities exceeding the fluid flow velocity $V > U \approx 0.6$ m/s, data of dendrite growth velocity from terrestrial and from reduced

gravity experiments coincide. The results of sharp interface modelling neglecting the influence of fluid flow are depicted in Figure 6 (solid line). It describes the experimental results obtained in reduced gravity. The sharp interface model regarding convection describes the experimental results obtained under terrestrial conditions if a fluid flow velocity, of $U \approx 1.2$ m/s, is assumed (*cf.* dashed line in Figure 6). At growth velocities $V > 0.6$ m/s, the computed relation of $V = f(\Delta T)$, without and with convection, converge to one line since, in this region, the dynamics of solidification is mainly limited by thermal diffusivity.

Figure 6. Dendrite growth velocity of B2 β-phase of $Al_{50}Ni_{50}$ alloy as a function of undercooling measured under terrestrial conditions (circles) and in reduced gravity (diamonds). The solid line represents the prediction of dendrite growth theory without convection and the dashed line with convection. *U* denotes the speed of fluid flow inside an electromagnetically levitated droplet as estimated by magneto-hydrodynamic simulations [45].

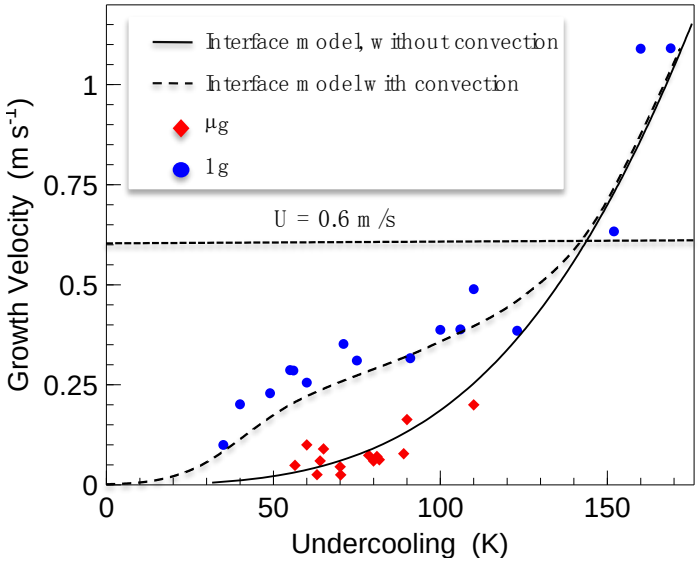

2.2.3. Deviations from Local Equilibrium during Rapid Dendrite Growth in Pure Ni

Pure metals show in general very large dendrite growth velocities which can range up to 100 m/s at large undercoolings $\Delta T \approx 300$ K [2]. Dendrite growth in pure metals is controlled, exclusively, by heat transport and atomic attachment kinetics at the solid-liquid interface. The curvature undercooling can be neglected since a thermal dendrite has a large curvature radius at its tip compared to alloys. This is caused by the fact that the thermal diffusivity is by orders of magnitude higher than the mass diffusion coefficient in alloys. As a consequence, the total undercooling of a pure metal can be approximated by the sum of thermal and kinetic undercooling, $\Delta T \approx \Delta T_T + \Delta T_K$. At small undercoolings, the thermal undercooling dominates while, at large undercoolings, the kinetic undercooling of the interface becomes dominant. Concerning the interface undercooling different cases can be distinguished.

According to Coriell and Turnbull atomic attachment kinetics at the solid-liquid interface of pure metals should be collision limited [46]. This means that the atomic vibration frequency, which is in the order of the Debye frequency (10^{13} Hz) in the liquid phase, shall give the limiting factor of atomic attachment kinetics and, therefore, the speed of sound will be the upper limit of growth velocity. Assuming collision, limited growth the kinetic growth coefficient should be $\mu = 2.77$ m/s/K for pure

Ni. Otherwise, atomic simulations of atomic attachment kinetics in pure metals suggest that thermally driven Brownian motion sets the upper limit of atomic attachment kinetics. In this case, the kinetic growth coefficient should be smaller by a factor of 5–6 [47], thus, $\mu = 0.5$ m/s/K.

In the case of diffusion-limited atomic attachment kinetics the kinetic growth coefficient should be even orders of magnitude smaller compared with collision-limited growth since the relaxation frequency for atomic diffusion is much less than the Debye frequency. Diffusion limited growth is observed in intermetallic compounds with superlattice crystal structure. In this case, atoms have to sort themselves out to find the proper lattice place. For this process, at least short-range diffusion is necessary. Diffusion limited growth has been reported first for FeSi and CoSi equiatomic intermetallic compounds [44]. Assuming diffusion controlled attachment kinetics in pure Ni, a kinetic growth coefficient of $\mu = 0.0069$ m/s/K is estimated. For comparison, atomic simulation of kinetic growth coefficients give for growth in 100 direction $\mu_{100} = 0.36$ m/s/K for pure Ni and $\mu_{100} = 0.015$ m/s/K for the equiatomic intermetallic compound AlNi, respectively [48]. These values are not directly comparable with the figures given above, but reveal, qualitatively, the decrease of the kinetic growth coefficient for collision-limited growth of pure Ni and diffusion-controlled growth for the intermetallic compound AlNi.

Figure 7. Dendrite growth velocity V as a function of undercooling ΔT, measured for pure Ni, using a Capacity Proximity Sensor, CPS (open circles) [49], a High Speed Camera (HSC) in terrestrial experiments (open diamonds) [11] and a High Speed Camera in reduced gravity experiments using the TEMPUS facility during parabolic flight campaigns (full squares) [50]. The lines give the predictions of dendrite growth theory assuming collision-limited growth (dashed), thermally limited growth (dotted) and diffusion limited growth (dash-dotted). The solid line gives a fit through the results obtained from microgravity experiments in which forced convection is neglected.

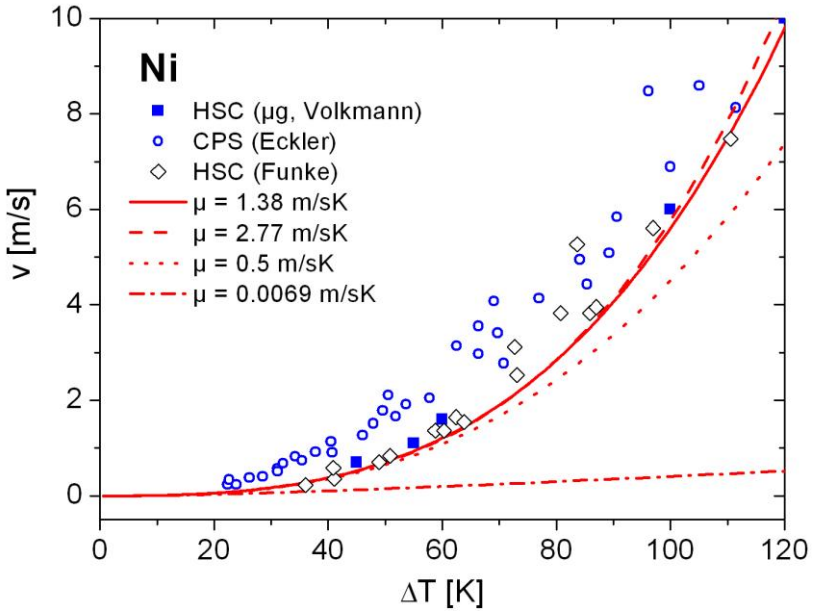

Figure 7 exhibits measurements of dendrite growth velocity, V, as a function of undercooling, ΔT, of pure Ni. The open circles represent results of measurements using the Capacity Proximity Sensor

(CPS) [49], the open diamonds give results of measurements using a High Speed Camera (HSC) [11]. Both sets of these experiments are performed under terrestrial conditions. In addition, the full squares exhibit results of measurements in reduced gravity using the TEMPUS facility (*cf.* Chapter 3.3) and the HSC [50]. These results scatter much less compared with the measurements under terrestrial conditions. Obviously, the measured values are significantly smaller in comparison with the CPS data measured under terrestrial conditions. This difference is attributed to the strong convection in electromagnetically levitated melts, which leads to an increase of the growth velocity, as described in the previous chapter. The lines represent results of calculations of the dendrite growth velocity within the sharp interface model. The dashed line corresponds to collision-limited growth, the dotted line to thermally controlled growth, the dash-dotted line to diffusion limited growth, and the solid line is a fit through the high accuracy data obtained in reduced gravity with negligible convection. The kinetic growth coefficient is used as fit parameter and yields a value close to the computed value assuming collision-limited growth. From these comparative investigations, it is concluded that the assumption of collision limited growth leads to a good description of dendrite growth in undercooled nickel.

2.2.4. Solute Trapping and Supersaturated Solid Solutions

In alloys chemical segregation plays an important role in microstructure evolution. This is because the solubility of the solute in the solvent is less in the solid state compared with the liquid state. As a consequence, solute will pile up in front of the solid-liquid interface during solidification under near equilibrium conditions. Only part of the solute can be dissolved in the solid phase with a concentration that is given by the equilibrium phase diagram. However, if the velocity of the growing dendrite is increased and is approaching the atomic diffusive speed solute will be trapped in the solid phase with a concentration that is beyond chemical equilibrium. If the growth velocity is exceeding the atomic diffusive speed, the fast growing dendrite stem will trap all solute and complete partition-less solidification occurs. The concept of solute trapping is schematically illustrated in Figure 8.

Figure 8. Illustration of solute partitioning at small dendrite growth velocity (**left**) and complete solute trapping at higher velocity (**right**). If the dendrite growth velocity V is less than the atomic diffusive speed V_D, solute atoms are segregating. In contrast if the growth velocity is larger than the atomic diffusive speed solute is trapped in the solid leading to solidification of a supersaturated solid solution.

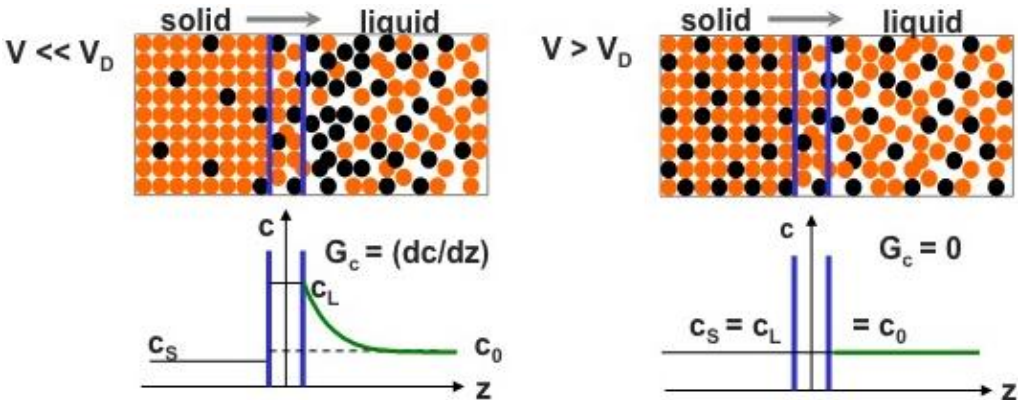

Solute trapping during rapid dendrite growth of undercooled melts has been demonstrated in previous investigations of both completely miscible solid solutions, such as Cu-Ni [51], and alloys with complex phase diagrams in the region of dilute concentration, such as $Ni_{99}B_1$ alloy [52]. This has been further supported by equivalent investigations on the dilute $Ni_{99}Zr_1$ alloy in which the dendrite growth velocity has been measured as a function of undercooling using the CPS. The diffusion coefficient, as one of the most important parameter in modeling dendrite growth, was independently determined by laser surface re-solidification experiments in combination with Rutherford backscattering experiments [53].

Figure 9 shows the dendrite growth velocity as a function of undercooling measured on $Ni_{99}Zr_1$, both by the Photo Diode Sensor technique (open symbols) and a High Speed Camera (closed symbols), respectively. The solid line represents results of dendrite growth modelling within the sharp interface theory [54]. The results found using the Photo Diode Sensor technique and the HSC system are matching. Due to methodical and technical improvements, the HSC measurements have lower experimental scatter.

Figure 9. Theoretical predictions (solid line) of the dendrite growth velocity *V vs.* the undercooling ΔT in comparison with (i) measurements using the Photo Diode technique (open squares) and with (ii) measurements using a High Speed Camera system (solid circles) for the dilute $Ni_{99}Zr_1$ alloy. At a critical point $\Delta T(V = V_D) = \Delta T^* = 198$ K, a transition from solutal and thermal growth to purely thermally controlled growth occurs and diffusion-less solidification begins to proceed at $\Delta T(V \geq V_D) \geq \Delta T^*$.

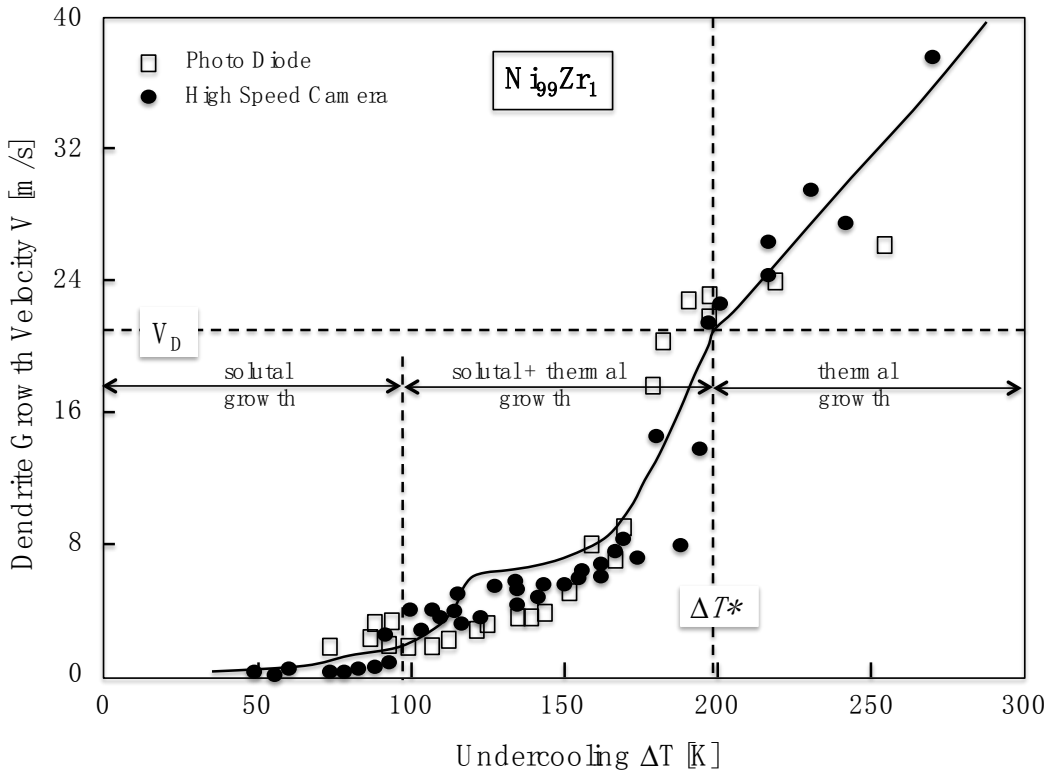

The experimental data on solidification of the $Ni_{99}Zr_1$ alloy cover a wide range of undercoolings up to $\Delta T = 271$ K and of dendrite growth velocities up to $V = 37.5$ m/s. They clearly exhibit an abrupt change in the solidification mechanism at a fixed critical undercooling ΔT^*, at which the dendrite tip

velocity is equal to the solute diffusion speed in bulk liquid, $V = V_D$. The sharp-interface model of dendritic growth is used to interpret the experimental results. The model attempts to describe: (i) diffusion-limited growth of dendrites (*i.e.*, growth of "solutal" dendrites at low undercoolings); (ii) diffusion-limited and thermally-controlled growth of dendrites (*i.e.*, growth of "solutal" and "thermal" dendrites in the intermediate range of undercoolings); and (iii) purely thermally-controlled dendritic solidification at higher undercoolings. The description of dendritic growth over the whole range of undercooling is made possible by introducing both deviations from local equilibrium at the interface, as well as in the solute diffusion field. Both contributions play an important role in high solidification velocities.

It can be seen from Figure 9 that sharp interface theory reasonably predicts three regimes for dendritic solidification in agreement with the experimental data. The first regime is described by the low-velocity branch predicted for chemical diffusion—limited growth. The second regime is transitive, and is characterized by growth of both solutal and thermal dendrites. The third regime occurs at higher undercoolings, consistent with $\Delta T(V) \geq \Delta T^*(V_D)$. This regime begins with an abrupt change in the kinetic curve at $\Delta T = \Delta T^*$, which can be explained by the end of the transition from solutal and thermal dendrites to thermal dendrites and the onset of diffusion-less dendritic growth. The first region ends at an undercooling of about $\Delta T \approx 90$ K. The second region covers the undercooling range $90 \text{ K} < \Delta T < 198$ K, while the third region starts at $\Delta T \approx 198$ K.

Figure 10. Microstructures of a dilute $Ni_{99}B_1$ alloy solidified from a melt undercooled by 60 K (**left**) and solidified upon an undercooling of 300 K (**right**). The microstructures have been received by neutron autoradiography technique that is extremely sensitive for boron detection. The distribution of boron is visible by the dark regions while nickel-rich regions appear bright. The left microstructure shows strong segregation of boron in the interdendritic regions while the right microstructure shows more or less homogeneous distribution of boron over the entire cross section [52].

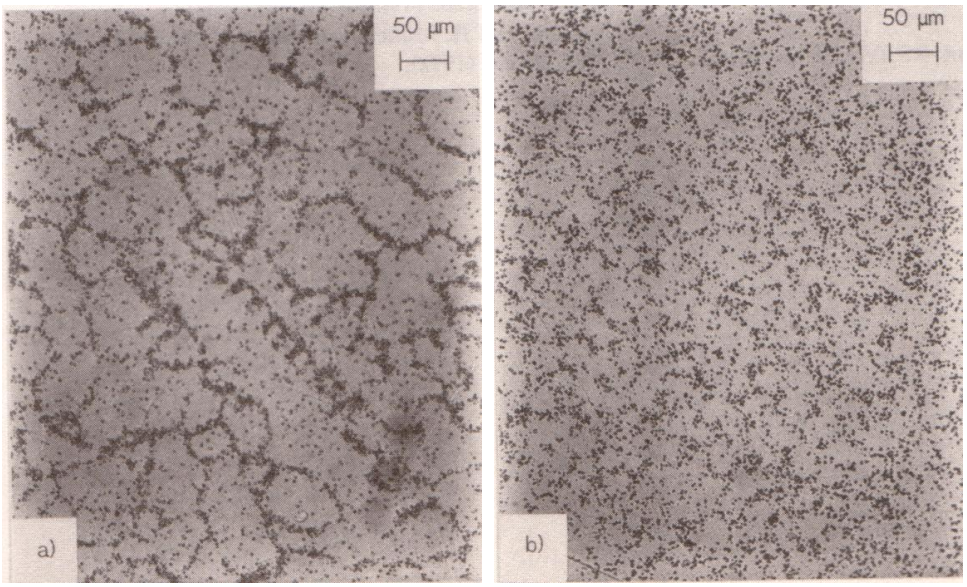

The sharp-interface model predicts an abrupt change in the growth kinetics with a break point at a critical undercooling ΔT^* and at a solidification velocity $V = V_D$ for the onset of the diffusion-less growth of crystals. Even though the dendritic growth velocity is reasonably predicted for the whole range of undercoolings, the theoretical curve overestimates the experimental data in the region of diffusion-limited growth with $\Delta T < 90$ K. One reason for such a disagreement might be the dependence of the solute partitioning and the diffusion coefficient on the temperature, and this dependence should be taken into consideration for future modelling work. The consequences of dendrite growth kinetics in undercooled melts of alloys on the microstructure evolution is demonstrated in Figure 10.

2.2.5. Disorder Trapping and Disordered Superlattice Structure

An analogous effect to solute trapping, disorder trapping [55] occurs during rapid crystallization of undercooled melts of *intermetallics* with superlattice structure. In such systems, crystal growth is very sluggish at small undercoolings [44]. The atomic attachment of atoms from the liquid to the solid needs short-range atomic diffusion, as atoms have to sort themselves out to find their proper lattice place in the superlattice structure. If undercooling increases the non-equilibrium effect of disorder, trapping leads to the solidification of a metastable disordered structure.

The mechanism of disorder trapping is schematically illustrated in Figure 11 for the equiatomic intermetallic $Al_{50}Ni_{50}$ alloy.

Figure 11. Schematic illustration of ordered growth forming an ordered superlattice structure at small dendrite growth velocity (**left**) disorder trapping at higher velocity leading to a disordered superlattice structure (**right**). Similar as for solute trapping the atomic diffusive speed is the essential parameter separating the regions of equilibrium and non-equilibrium crystallization.

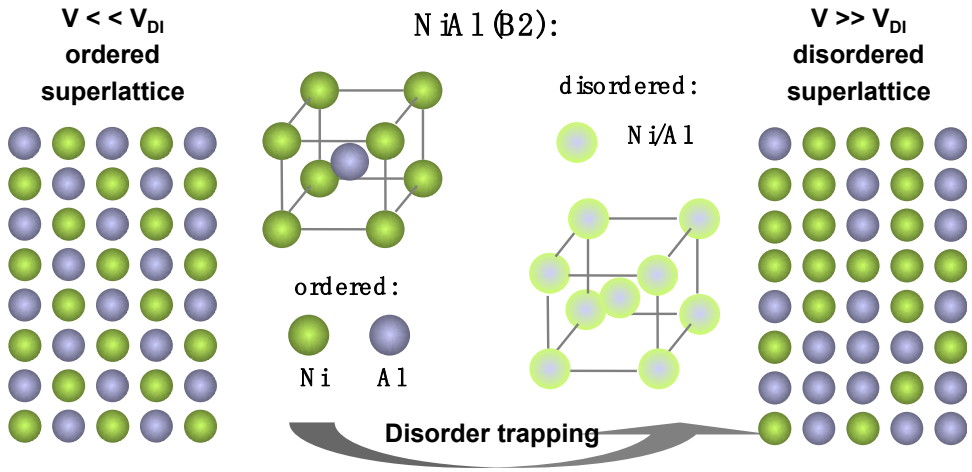

Measurements of the dendrite growth velocity of intermetallic phases exhibit a steep rise in the growth velocity *versus* undercooling relation at a critical undercooling ΔT^*. This change of the dendrite growth kinetics has been attributed to a transition from ordered to disordered growth of superlattice structures [56–58]. However, for $Ni_{50}Al_{50}$ diffraction experiments on the as-solidified samples at ambient temperatures failed to prove a disordered superlattice structure [57]. This result

was explained by transformations of primary solidified disordered structures to stable ordered phases during the post-recalescence and the post-solidification period [58]. It was shown that metastable disordered phases transform to the ordered state on a rather short time scale [59]. Transmission electron microscopy on rapidly solidified Ni-Al intermetallic alloys reveal antiphase domains, which indicate the occurrence of disorder trapping during crystallization of drop tube processed melts [60] and rapid laser surface re-solidification of Ni-Al intermetallic phases [61]. During pulsed laser melting studies on Ni_3Al, a disordered fcc phase has been quenched in although an ordered $L1_2$ phase is stable up to the melting temperature, providing direct evidence of disorder trapping during non-equilibrium solidification [62]. Nevertheless, these studies provide no direct experimental link between the occurrence of disorder trapping and the growth velocity-undercooling relationship.

Figure 12 shows the results of measurements of dendrite growth velocity as a function of undercooling for the intermetallic $Ni_{50}Al_{50}$ alloy. The measured growth velocities continuously increase with undercooling. If the undercooling exceeds a value of $\Delta T^* \approx 250$ K, a steep rise of V is observed. At smaller undercoolings, the growth velocities are of the order of about 1 m/s or even less, this is comparable with fluid flow in electromagnetically levitated drops (*cf.* Figure 6). The intermetallic $Ni_{50}Al_{50}$ alloy melts congruently. Hence, mass transport by mass redistribution and, consequently, constitutional effects can be neglected, therefore, the constitutional undercooling $\Delta T_c \approx 0$. Due to the large curvature radius of thermal dendrites, the curvature undercooling can be equally neglected. Therefore, the thermal undercooling and the kinetic undercooling control the dendrite growth kinetics of the intermetallic $Al_{50}Ni_{50}$ compound.

Figure 12. Top: Dendrite growth velocity V as a function of undercooling ΔT measured by use of a high-speed video camera (full circles) and computed by applying the sharp interface model, with (solid line) and without (dashed-dotted line), taking into account small constitutional effects due to the shift of the congruent melting point in the kinetic phase diagram. If any constitutional contributions are neglected the temperature characteristics of $V(\Delta T)$ does not change with the exception that the sharp increase of V sets in at a critical undercooling, being about 25 K smaller (dashed-dotted line). Bottom: The order parameter η is shown as a function of undercooling as inferred from the analysis of the experimental results.

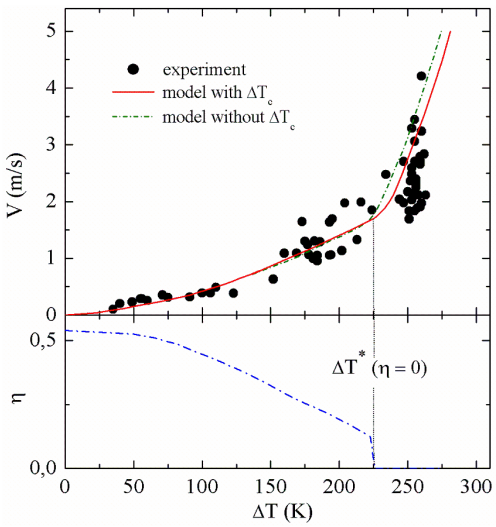

The results of the measured dendrite growth velocities are analysed within the sharp interface model introduced in Chapter 2.2.1. In addition to the system of equations given by this model, the non-equilibrium effect of disorder trapping has to be introduced in this concept. In order to so, we combine the sharp interface theory with a model of disorder trapping, as developed by Boettinger and Aziz [55] that has been extended by Assadi and Greer [63]. This approach bases on the thermodynamic description in which the Gibbs free energy of the liquid, G_L, is expressed by a regular solution model and that of the solid intermetallic phase, G_S, is expressed as a function of the order parameter, η. η is defined by the difference of the fractions of atoms located in the correct and the wrong places within the superlattice of the ordered B2 structure. The link between non-equilibrium thermodynamics and crystal growth is established by three kinetic equations. One of these equations is the growth equation by Wilson and Frenkel:

$$V = V_0\left(1-\exp\frac{-\Delta G_{LS}}{k_B T}\right) \tag{19}$$

with $\Delta G_{LS} = G_L - G_S$. The solidification of the congruently melting intermetallic phase of $Ni_{50}Al_{50}$ requires no long-range diffusion. Collision limited growth for the atomic attachment kinetics of atoms from the liquid to the solid is assumed so that the kinetic prefactor V_0 is approximated by the velocity of sound V_S. For sorting of the atoms on the different sublattices, however, diffusion within the solid-liquid interface is required, which is governed by the speed of interface diffusion V_{DI} and by diffusion in the bulk liquid, V_D, which are two to three orders of magnitude smaller than V_S. The balance of the mass fluxes to the different sublattices of the more or less ordered solid phase during crystal growth defines two other kinetic equations [55,58]. Apart from thermodynamic and kinetic parameters, the equation system depends on five variables. These are the temperature of the solid-liquid interface T_i, the composition of the solid, x_s, and of the liquid phase, x_l, the order parameter η, and the growth velocity V. For a given V and at a fixed x_l, the other three variables, x_s, T_i and η can be determined by numerically solving the equation system. Hence, the model provides a description for the velocity dependence of the order parameter η(V). Moreover, by linking x_l, x_s, and T_i, it allows for calculating a metastable phase diagram in which the liquidus temperature line depends on the velocity V, thus, $T_L(V)$. From this kinetic phase diagram, the kinetic undercooling ΔT_K (difference between local equilibrium liquidus and velocity dependent liquidus temperature), $k(V)$ and $m(V)$ are directly inferred. More details of the computations are given in [64].

The results of the computations of dendrite growth velocity as a function of undercooling are given in the upper part of Figure 12 (solid line). It is evident that the predictions of the extended sharp interface model are in reasonable agreement with the experimental results over the entire range of undercooling accessible by application of the electromagnetic levitation technique.

At large undercoolings the model reproduces the sharp increase of V at ΔT^*. Small constitutional effects by the slight shift of the congruent melting point in the kinetic phase diagram are taken into account in the present calculations. If these constitutional effects are neglected, the critical undercooling at which V steeply rises is slightly shifted to lower undercoolings (*cf.* dashed-dotted line in Figure 12). The variation of the order parameter η with undercooling as predicted by the model of disorder trapping [55] is shown in the lower part of Figure 12. It continuously decreases with increasing undercooling and drops suddenly to zero at an undercooling at which disorder trapping sets

in as indicated by the sharp increase of dendrite growth velocity in the upper part of Figure 12. Even for small velocities, the order parameter is considerably smaller than 1 because some degree of disorder is favourable at elevated temperatures due to the entropic term in the Gibbs free energy.

The question may arise whether the disordered superlattice structure which is formed upon large undercoolings $\Delta T > 270$ K prior to solidification is preserved during cooling to ambient temperature. Since the transition from disordered to ordered phase takes place rapidly [59], a primarily formed disordered B2 phase is not necessarily present in the as solidified sample. In order to obtain unambiguous evidence of the formation of a metastable disordered phase during rapid solidification of the deeply undercooled melts Energy Dispersive X-ray Diffraction (EDXD) has been conducted on levitation processed $Al_{50}Ni_{50}$ alloys using synchrotron radiation at the European Synchrotron Radiation Facility (ESRF) in Grenoble [64].

Figure 13 (left) shows the results of EDXD on a levitation processed $Ni_{50}Al_{50}$ sample undercooled by 235 K prior to solidification. That is less than the critical undercooling, $\Delta T^* \approx 250$ K, at which the abrupt increase of V is observed. In the top left part the temperature-time profile recorded during the experiment cycle is shown. The sample was molten and subsequently heated to a temperature above the liquidus temperature of $T_L = 1949$ K. Subsequently, it is cooled and undercooled. At a temperature $T_N = 1714$ K, corresponding to an undercooling of $\Delta T = 235$ K, nucleation and subsequent growth of a solid phase occurs that leads to a rapid temperature rise due to the release of the heat of fusion during rapid solidification (recalescence). Then, the sample solidifies during the post-recalescence period and is cooled to ambient temperatures. The bottom left part of Figure 13 exhibits three diffraction spectra recorded during the time intervals as indicated in the temperature-time profile; A: on the undercooled liquid, B: during recalescence, and C: after solidification of the liquid. Spectrum B is acquired in a time interval of 1 s. Spectra B and C indicate that the thermodynamically stable ordered $Ni_{50}Al_{50}$ compound of B2 structure is directly formed during solidification. The same phase selection is observed for experiments in which smaller undercoolings ($\Delta T < 235$ K) are obtained. It is emphasized that, in all these cases, the (1,0,0) peak of the ordered B2 phase has been detected immediately after recalescence in a reproducible way.

Figure 13 (right) shows equivalent results of EDXD measurements on a $Ni_{50}Al_{50}$ sample which, however, is undercooled by an amount of $\Delta T = 255$ K that is larger than ΔT^* at which the temperature characteristics of the growth dynamics suddenly changes. Again, three spectra are depicted; A: on the undercooled liquid, B: during the recalescence, and C: after the solidification. Here, a phase is formed from the liquid (spectrum A) that shows only the (1,1,0) reflection of the NiAl intermetallic compound. However, the (1,0,0) diffraction peak is missing that represents the superlattice structure of the ordered B2 phase. Obviously, a metastable disordered NiAl intermetallic compound is formed during rapid solidification due to disorder trapping, if the melt is undercooled beyond $\Delta T^* \approx 250$ K. A few seconds later, this metastable disordered phase transforms to the stable ordered B2 phase as indicated by the occurrence of the (1,0,0) reflection in spectrum C, which results from the ordering of the as-solidified disordered superlattice structure during the post-recalescence period. Comparing both sets of EDXD experiments, it is evident that in fact the change in the temperature characteristics of the growth velocity—undercooling relation $V(\Delta T)$, at $\Delta T^* \approx 250$ K is caused by disorder trapping during rapid dendrite growth in the undercooled melt.

Figure 13. Temperature-time profiles (upper part) and EDXD spectra (lower part) measured during solidification of a $Ni_{50}Al_{50}$ melt at an undercooling of ΔT = 235 K (**left**) and ΔT = 255 K (**right**). The arrows in the temperature-time profiles indicate the time intervals during which the X-ray diffractograms A, B, C were acquired. Note that the Bragg peak indexed by β (1,0,0), which corresponds to the superlattice structure of ordered B2 phase is missing on trace B on the right hand side.

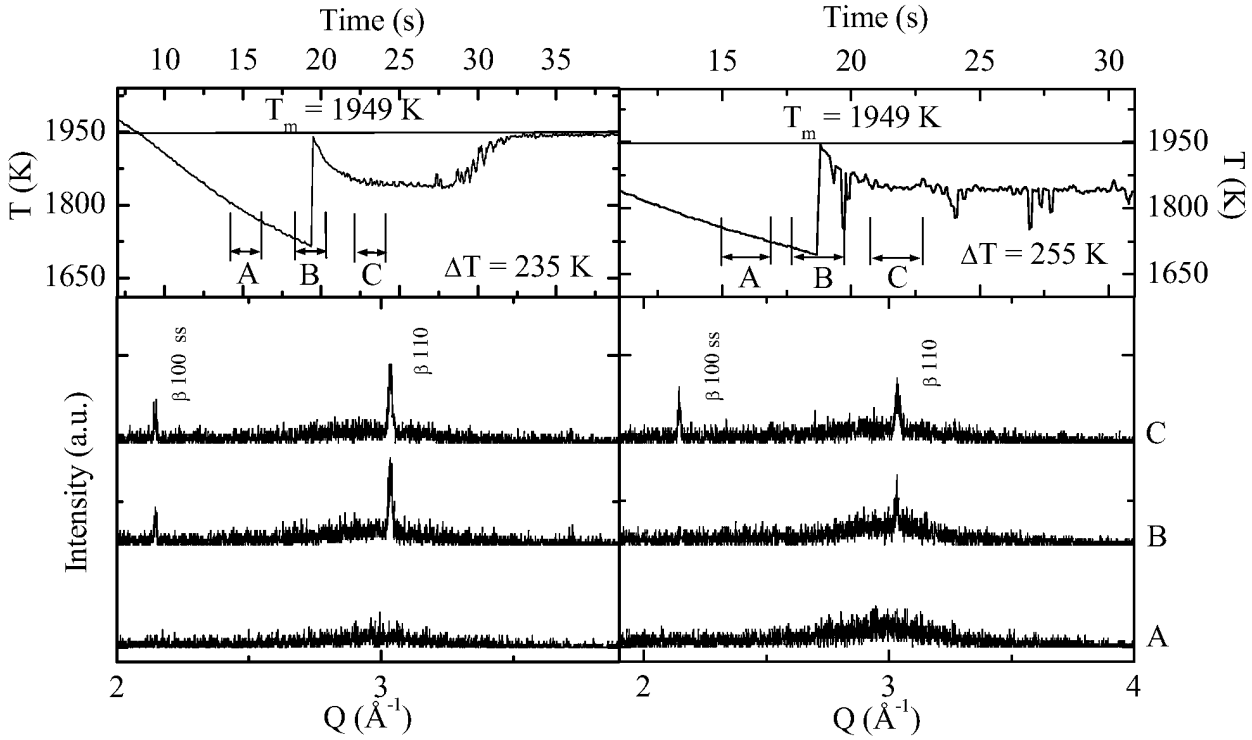

2.2.6. Dendrite Growth in Undercooled Glass-Forming $Cu_{50}Zr_{50}$ Alloy

Thus far, the majority of the measured velocity-undercooling (V-ΔT) relations in metallic systems show a monotonous increase of V with ΔT. In this case the energetics controls the growth [65]. In glass-forming systems, however, the mobility of the atomic movement rapidly decreases if ΔT is approaching $\Delta T_g = T_L - T_g$. The steeply decreasing diffusion coefficient eventually overcomes the acceleration of the interface due to the increase of the thermodynamic driving force for crystallization, the Gibbs free energy difference $\Delta G = G_l - G_s$ with G_l and G_s the Gibbs free energy of liquid and solid, respectively. This leads to a maximum in the V-ΔT relation. This was experimentally observed in a great variety of non-metallic glass-forming systems, such as *o*-terphenyl [66], tri-α-naphthylbenzene [67], Li_2O-$2SiO_2$ [68], and MgO-CaO-$2SiO_2$ [69]. However, thus far, there is only one work that reports a maximum in the V-ΔT relation measured for the $Cu_{50}Zr_{50}$ glass-forming alloy [32].

The results of the measurements of V as a function of ΔT are shown in Figure 14. The squares give the experimental data. Taking the values of the melting temperature and the glass temperature of $Cu_{50}Zr_{50}$, the difference between T_l = 1209 K and T_g = 670 K, is determined as ΔT_g = 539 K. This corresponds to a relative glass temperature T_g/T_l = 0.56 [70]. Such a high value is indicative for an excellent glass forming ability [17]. A maximum in the V-ΔT relation is experimentally observed. It indicates that, at undercoolings less than the undercooling of the maximum growth velocity, dendrite

growth is controlled by the thermal transport, while at undercoolings larger than the undercooling of the maximum growth velocity, dendrite growth is governed by atomic diffusion. The maximum undercooling achieved in the experiment is approaching the temperature range above the glass temperature where the rapidly decreasing diffusion coefficient increasingly influences the atomic attachment kinetics and, thus, the mobility of the solidification front

Figure 14. Measured growth velocity V as a function of undercooling ΔT (squares). There is a specific undercooling: At ΔT^* = 144 K the thermal undercooling ΔT_t equals to the kinetic undercooling ΔT_k, The solid line gives the prediction of dendrite growth theory assuming diffusion-limited growth and taking into account a temperature dependent diffusion coefficient (see the text).

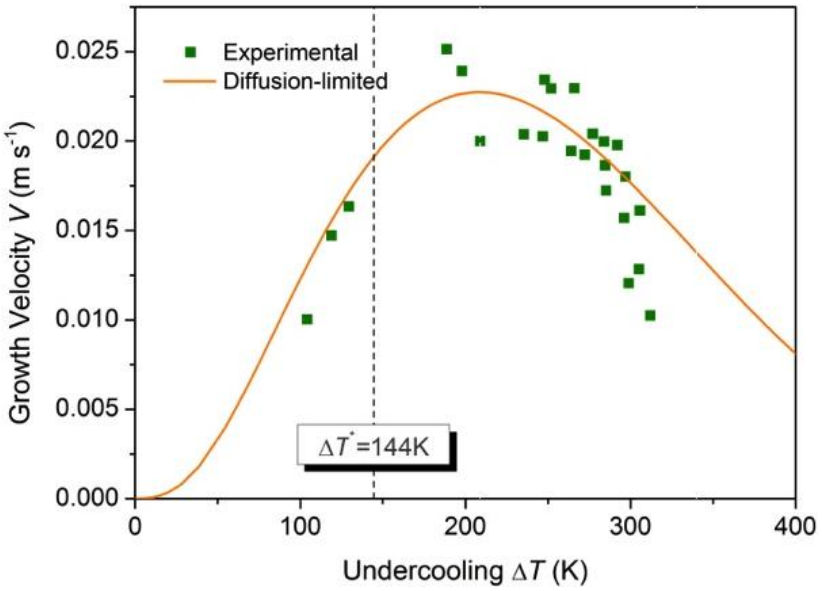

The experimental results are analysed within the sharp interface model, as described in Chapter 2.2.1. Taking into account the temperature dependence of the diffusion coefficient extends this model. The $Cu_{50}Zr_{50}$ is an intermetallic compound, which melts congruently. Therefore, constitutional contributions to the undercooling can be excluded similar as in the case of $Al_{50}Ni_{50}$ compound discussed in a previous chapter. In addition, the curvature undercooling is neglected because this contribution is small for thermal dendrites with their large curvature radius at the tip. Therefore, the total undercooling is approximated by $\Delta T \approx \Delta T_T + \Delta T_K$. The kinetic undercooling, ΔT_K, is controlled by the atomic attachment kinetics at the solid-liquid interface. In case of an intermetallic compound, such as $Cu_{50}Zr_{50}$, and even more because of the good glass-forming ability of this alloy the atomic attachment kinetics will be diffusion controlled. In this case, the prefactor V_o in equation (19) shall correspond to the atomic diffusive speed, V_d. Equation (19) is then rewritten as:

$$V = V_D\left(1-\exp\left(-\frac{\Delta G_{LS}}{k_B T}\right)\right) \text{with } V_D = CD_l = CD_o \exp\left(-\frac{Q_D}{R_g T_i}\right) \quad (20)$$

where $D_l(T)$ is the temperature dependent diffusion coefficient in the liquid and Q_d is the activation energy for diffusion. This is the case when ordering in the liquid [71,72] is necessary for crystallization [73]. The activation energy of crystallization in a number of metals and alloys is the

same as for diffusion [74]. Obviously, the diffusion-limited crystallization mode prevails even in pure metals at large undercoolings, e.g., it seems thermally-limited for Ag at low ΔT [75] but is actually diffusion-limited on the whole for ΔT up to ΔT_g [76]. According to Aziz and Boettinger [56], the pre-factor C in Equation (20) is defined as $C = f/\lambda$ with λ the interatomic spacing and f a geometrical factor of order unity. If λ (=1.98 Å) is given as the average lattice spacing normal to (100) and (110) surfaces in the MD simulation [77], the inter-diffusion coefficient $D_l = V_o\lambda/f$ can be determined.

For further analysis, each experimental point is fitted with the dendrite growth model to obtain the upper limit of the growth velocity V_0 at each measured undercooling ΔT. V_0 is then plotted as a function of $1000/T_i$ in a semi-logarithmic diagram, as shown in Figure 15. It is interesting to see that the evolution of V_0 with T_i follows the Arrhenius law except for the last three experimental points at high ΔT. This means that crystallization of $Cu_{50}Zr_{50}$ melt is thermally activated with a prefactor CD_o = 1425.8 m/s and an activation energy $Q_D = 79759\frac{J}{mol} = 0.827\ eV$. Based upon these results, the dendrite growth velocity V is calculated as a function of the total undercooling ΔT. The results of these computations are presented by the solid line in Figure 14. The experimental results of the dendrite growth velocity are well reproduced. A maximum V = 0.227 m/s is found at ΔT = 209 K which is quite close to the experimental measurement of a maximum V = 0.025 m/s at ΔT = 200 K. It is interesting to note that using the temperature dependent viscosity does not lead to a matching of the experiments and the modelling [32], in contrast to the present work where the temperature dependent diffusion coefficient is used to take into account the mobility of the solid-liquid interface. This may be understood by the fact that the Einstein-Stokes relation does not hold for Zr-based glass forming alloys [78].

Figure 15. Arrhenius plot of the upper limit of growth velocity V_0 as a function of 1000 times the reciprocal interface temperature $1000/T_i$: experimental data (squares); results of the computations (solid line).

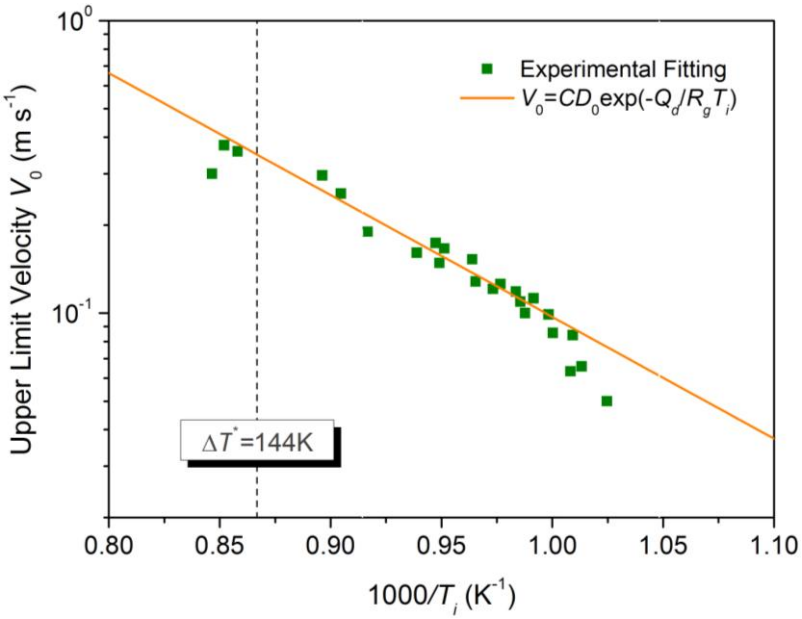

As to a similar undercooled glass-forming $Ni_{50}Zr_{50}$ alloy, from which a stoichiometric compound NiZr is crystallized, the self-diffusion coefficient of Ni D_{Ni} was measured [79]. The activation energy

for the atomic diffusion is determined as $Q_d = 0.73 \pm 0.03$ eV which is very close to the value inferred from the slope of the computed line in Figure 15, $Q_d = 0.827$ eV. If D_{Ni} is extended to low temperatures, there are no large differences between D_{Ni} and the current result inferred from the dendrite growth measurements in undercooled $Cu_{50}Zr_{50}$ alloy. The temperature dependent self-diffusion coefficients of Cu, D_{Cu} and, Zr, D_{Zr} were investigated by MD simulations for $Cu_{50}Zr_{50}$ [80]. The activation energies, as determined from these results, lead to the activation energies of the atomic self-diffusion for Cu and Zr, $Q_{Cu} = 0.42$ eV and $Q_{Zr} = 0.44$ eV. Despite potential significant uncertainties due to the difference in the interatomic potentials, the current diffusion coefficient and its activation energy are within the uncertainty of MD simulation results. Thus, it is quite reasonable to conclude that crystallization of undercooled $Cu_{50}Zr_{50}$ alloy is diffusion-limited through the undercooling range where the interface undercooling is dominant. The deviations at high ΔT (Figures 14 and 15) are attributed to two effects. First, the anisotropy effect of the kinetic coefficient which is quite important for selecting the operating state of the dendrite [81] especially at high ΔT is not considered in the solvability theory. Second, the diffusion changes from a thermally activated single atom to a more collective atomic mechanism when the temperature of the undercooled melt approaches the glass temperature, $T \rightarrow T_g$, and the Arrhenius law does not hold at very high ΔT [82,83].

3. Levitation Techniques

3.1. Electromagnetic Levitation

For metallic systems the most suitable technique for freely suspending spheres of diameter up to 1 cm is the electromagnetic levitation technique. Figure 16 shows an electromagnetically levitated sphere in a levitation coil. The principle of electromagnetic levitation is based on the induction of eddy currents in an electrically conducting material if the material experiences a time dependent magnetic field B (Lenz rule):

$$\nabla \times E = -\partial B / \partial t \tag{21}$$

with E the electrostatic field. For a non-uniform magnetic field the eddy currents induced in a sample produce a magnetic dipole moment m that is opposite to the primary field B. This leads to a diamagnetic repulsion force F_r:

$$F_r = -\nabla(m \cdot B) \tag{22}$$

between the primary field und the sample. If the repulsion force F_r is equal in amount and opposite in direction to the gravitational force, $F_r = m_g \cdot g$, the sample is levitated. m_g denotes the mass of the sample and g the gravitational acceleration. Electromagnetic levitation can be used to levitate metallic and even semi-conducting samples. However, electromagnetic levitation of semiconductors requires either doping with a metallic element to increase the electrical conductivity or preheating the pure semiconductor to a temperature of about 1000 K by a laser or by a graphite susceptor within the levitation coil so that the intrinsic conduction is sufficiently increased to electronically couple the sample to the alternating external field. A characteristic feature of electromagnetic levitation is that both levitation and heating of the sample are always occurring simultaneously. This offers the

advantage that no extra source of heating is required to melt the material, but it is associated with the disadvantage that levitation and heating can only be controlled independently in a very limited range.

Figure 16. Schematics of electromagnetic levitation; the droplet is placed in a levitation coil consisting of four water cooled windings and two counter windings at the top to stabilize the position of the levitated drop. Two infrared pyrometers measure contactless the temperature of the droplet from the top and from a radial side. A high-speed camera is used to observe the rapid propagation of the solidification front. Cooling gas from the top is necessary to remove the heat from the sample to be cooled and undercooled. This is achieved by a high thermal conductivity gas like He. The arrows give the geometry of the magnetic field inside the coil. F_L and F_g denote the levitation force and the gravitational force while I_c is the current induced in the droplet by the alternating electromagnetic field.

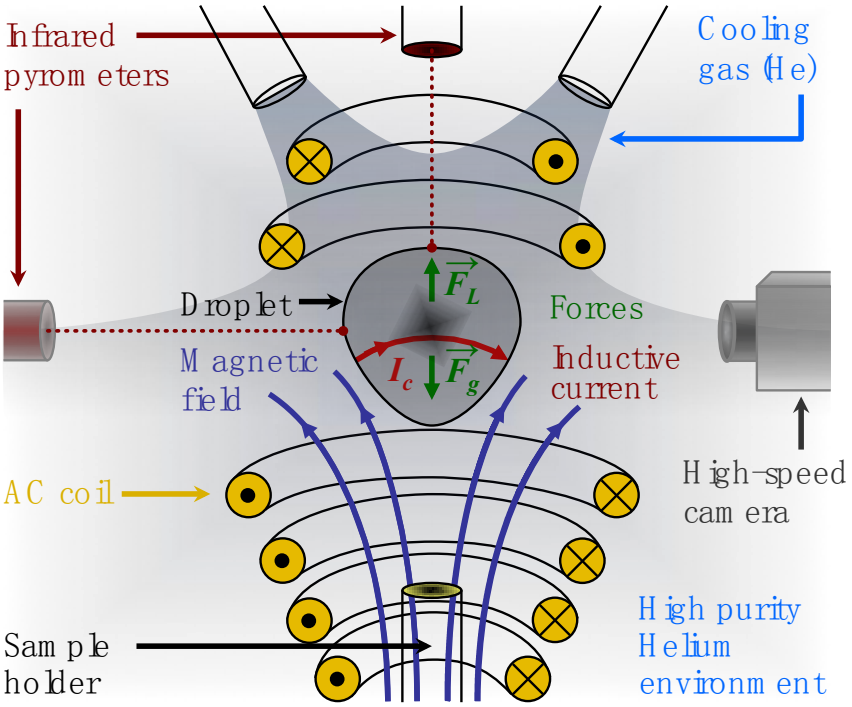

According to Rony [84], the mean force on an electrically conductive non-ferromagnetic sample is determined by:

$$F_{em} = -\frac{4\pi r}{3} \cdot \frac{B \cdot \nabla B}{2\mu_o} \cdot G(q) \tag{23}$$

Here, r denotes the radius of the sphere-like sample, μ_o the permeability of vacuum. The function $G(q)$ is calculated as:

$$G(q) = \frac{3}{4}\left(1 - \frac{3\sinh(2q) - \sin(2q)}{2q\cosh(2q) - \cos(2q)}\right) \tag{24}$$

q is the ratio of the sample radius and the skin depth δ:

$$q = \frac{r}{\delta} \text{ with } \delta = \sqrt{\frac{2}{\mu\omega\sigma}} \tag{25}$$

ω, σ, and μ are the angular frequency of the electrical current, the electrical conductivity and the magnetic permeability of the sample, respectively. According to equation (23), the levitation force scales with the gradient of the magnetic field. To optimize levitation, it is therefore crucial to design properly the geometry of the levitation coil and optimize the function $G(q)$. The efficiency of electromagnetic levitation is adjusted by the parameters of the frequency of the alternating electromagnetic field, the sample size and the electrical conductivity of the sample. For a vanishing conductivity, ($q \to 0$) $G(q)$ becomes zero and levitation is not possible as $q \to \infty$ $G(q)$ is approaching saturation.

To levitate a sample of mass m the gravitational force F_g has to be compensated by the electromagnetic levitation force F_{em}:

$$F_{em} = -F_g,\ F_g = m \cdot g = \frac{4\pi r^3}{3}\rho \cdot g \tag{26}$$

where ρ denotes the mass density of the material. The z-component of the force follows as:

$$\frac{\partial B^2}{\partial z} = \frac{2\mu_o g}{G(q)} \cdot \rho \tag{27}$$

For a given magnetic field and sample size, the levitation force is determined by the skin depth δ and the mass density m. The mean power absorption P is calculated according to Roney [83] as:

$$P = \frac{B^2}{2\mu_o} \cdot \omega \cdot \frac{4\pi r^3}{3} \cdot H(q) \tag{28}$$

with:

$$H(q) = \frac{9}{4q^2} \cdot \left(q \cdot \frac{\sinh(2q) - \sin(2q)}{\cosh(2q) - \cos(2q)} - 1 \right) \tag{29}$$

$H(q)$ is the efficiency of the power absorption. For vanishing electrical conductivity no power is absorbed by the sample. On the other hand, for an ideal conductor no ohmic losses occur so that $H(q)$ converges to zero.

The temperature control of electromagnetically levitated samples requires a separate action of P and F_{em} as far as possible. The essential difference between P and F_{em} is that the functions $G(q)$ and $H(q)$ have a different characteristics with respect to the frequency of the alternating electromagnetic field: F_{em} depends on the product $(B\bullet\nabla)B$, while P is proportional to B^2 (*cf.* Equations (23) and (28)). Hence, temperature control is possible within a limited range by choosing a proper frequency of the alternating field and by a movement of the sample along the symmetry axis of a conically shaped coil. In the lower regions of the coil, the windings are tighter, thus, the magnetic field and power absorption are greater than in the upper region of the coil with lower field strength. By increasing the power, the sample is lifted up into regions of larger field gradients and smaller magnetic field strength and cools down [77].

3.2. Electrostatic Levitation

Electromagnetic levitation requires sample material that is electrically conductive. Therefore, the application of electromagnetic levitation is restricted to metals and (doped) semiconductors. The

advantage of electrostatic levitation is that levitation and heating is decoupled and the samples can be processed under ultra-high vacuum conditions provided the vapour pressure of the processed material is small. However, there is a problem with the stability of the sample position. According to the theorem of Samuel Earnshow, it is not possible to levitate a charged sphere within a static electrostatic field [85].

Electrostatic levitation is based on the Coulomb forces acting on an electrically charged sample in a quasi-static electrical field [86]. A sample with a surface charge q and a mass m is levitated against gravity within a static electrostatic field $\vec{E}$ as:

$$\vec{E} = -\frac{mg}{q} \cdot \vec{e}_z \tag{30}$$

$\vec{e}_z$ is the unit vector in z direction, *i.e.*, parallel to the electrostatic field. A stable position of the sample is based on a local potential minimum at $\vec{r}_o$ for all directions in space.

$$\frac{\partial^2}{\partial x^2}\Phi(\vec{r}_o) + \frac{\partial^2}{\partial y^2}\Phi(\vec{r}_o) + \frac{\partial^2}{\partial z^2}\Phi(\vec{r}_o) = \Delta\Phi(\vec{r}_o) > 0 \tag{31}$$

The Maxwell-equation for Gauss's law affords:

$$\Delta\Phi = -\frac{\rho}{\varepsilon_o} \tag{32}$$

Under vacuum conditions, $\Delta\Phi = 0$. Hence, a potential minimum does not exist and a stable sample position under stationary conditions is not possible. This means electrostatic levitation requires a sophisticated dynamic sample position and electrostatic field control. This became possible since the 1990a, when high voltage amplifiers were developed, which can be controlled with high slew rates of changing the voltage U, $dU/dt > 400$ V/μs.

Figure 17 shows schematically the active sample positioning system. An electrically charged sample is levitated between two horizontal electrodes within a widened positioning laser beam filling the whole space between the electrodes. The sample shadow is detected by a two-dimensional photo-sensitive detector that gives information on the vertical and horizontal position of the sample. A real time computer control algorithm developed by Tilo Meister [87] reads this information and adjusts instantaneously the voltage of the amplifier. In order to control the sample position in all three-dimensional directions, two positioning lasers perpendicular to each other and an assembly of six electrodes are used.

Two central electrodes, arranged as a plate capacitor, are surrounded by four electrodes in plane, which are cross-linked with the positioning lasers to push the sample in the central position. The forces acting in z-direction, $F(z)$, are the gravitational force, the force due to the electrical field, and the force between the sample and the grounded centre electrodes. With the method of image charges the force of a charged sphere between the electrodes can be determined by:

$$F(z) = \frac{q^2}{4\pi\varepsilon_o}\left(\sum_{n=1}^{\infty}\frac{1}{\left(2d_z n - 2z\right)^2} - \sum_{n=0}^{\infty}\frac{1}{\left(2d_z n - 2z\right)^2}\right) \tag{33}$$

with the position of the sample z, the distance of the electrodes d_z, the charge q of the sample, the vacuum permittivity ε_o, and the number of reflections n. Neglecting multiple reflections, $F(z)$ is approximated as:

$$F(z) \approx -\frac{q}{4\pi\varepsilon_o}\left(\frac{1}{(2z)^2}-\frac{1}{(2d_z-2z)^2}\right) \tag{34}$$

In the middle of the electrodes the forces of the image charge acting on the sample are compensating each other. The equation of motion for the z direction is given by: $mz = -m\ddot{g} - q\frac{U_z}{d_z} - \frac{q^2}{4\pi}$

$$m\ddot{z} = -mg - q\frac{U_z}{d_z} - \frac{q^2}{4\pi_o}\left(\frac{1}{(2z)^2}-\frac{1}{(2d_z-2z)^2}\right) \tag{35}$$

The field in x-direction and y-direction are assumed to be between two parallel electrodes:

$$m\ddot{x} = -2q\frac{1}{\kappa}\cdot\frac{U_x}{d_x} \quad \text{with} \quad \kappa = \sqrt{\left(\frac{2z}{d_x}\right)^2+1} \tag{36}$$

κ is a geometrical factor regarding the distance of the sample and the lateral electrodes.

Figure 17. Sketch of the fully automated active sample positioning system.

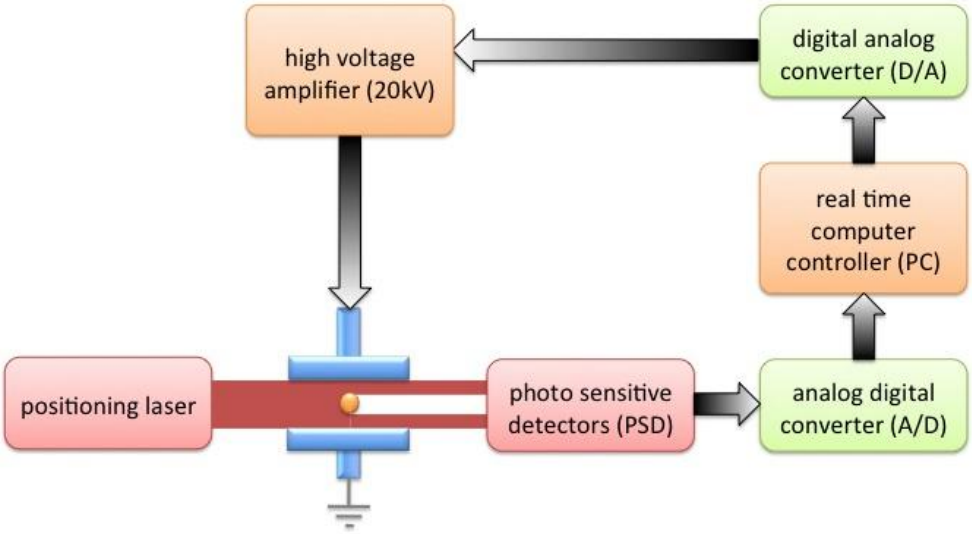

For conducting an experiment using the electrostatic levitator, the sample in diameter of about 2–4 mm is placed at the lower electrode, which is grounded. The high voltage power supply is switched on and immediately an electrostatic field between upper and lower electrode in z-direction is built up. At the same time, the sample is charged. Since the upper electrode is on negative potential, the surface of the sample is loaded with positive charge q^i that is calculated as [88]:

$$q^i = 4\pi\varepsilon_o L\frac{U_z}{d_z}r^2 \tag{37}$$

with r the radius of the sample and L = 1.645 a geometrical factor. The image charge of the bottom electrode dominates the initial levitation voltage. The force acting on a sample while lifting is given by:

$$F_z^i = \frac{4}{3}\pi r^3 \rho g - q\frac{U_z^i}{d_z} - \frac{q^2}{4\pi\varepsilon_o}\cdot\frac{1}{(2r)^2} = 0 \tag{38}$$

Combining Equations (37) and (38) yields the initial voltage for levitation:

$$U_z^i = \pm d_z\sqrt{\frac{4\rho g r}{3L(4-L)\varepsilon_o}} \tag{39}$$

The charge of the sample in the beginning of the experiment is then:

$$q^i = \mp 8\pi\sqrt{\frac{L\varepsilon\rho g r^3}{3(4-L)}} \tag{40}$$

The voltage U_z^o needed to keep the sample in the middle of the electrodes is calculated as:

$$U_z^o = \frac{4-L}{4}U_z^i \tag{41}$$

The initial voltage is larger than the voltage that is needed to levitate the sample in the middle of the horizontal electrodes. For a constant initial voltage, the time is approximated which elapses until the sample hits the electrode. This time is used to estimate the minimum sampling rate required for positioning. For a silicon sample with a diameter of 2 mm, the sampling rate is 2×10^{-3} s.

Electrostatic levitation offers the advantage that positioning and heating are decoupled in contrast to electromagnetic levitation. Heating is realized in electrostatic levitation by an infrared laser. Increasing the temperature of the sample leads to an evaporation of surface atoms, which is useful for undercooling experiments since the evaporation cleans the surface and, thereby, reduces, or even eliminates heterogeneous nucleation motes at the surface of the sample. On the other hand, the sample surface looses surface charge by evaporation. Therefore, the voltage has to be increased to keep the sample levitated. To facilitate recharging of the sample during levitation, a focused ultra violet light source with a high energy of several eV (λ = 115–350 nm) is used. In addition to this procedure, the sample is also recharged at elevated temperatures by thermionic emission of electrons [89].

3.3. Electromagnetic Levitation in Reduced Gravity

The application of electromagnetic levitation on Earth is limited by several restrictions. The strong electromagnetic fields needed to compensate the gravitational force cause strong stirring effects in the liquid and, hence, disturb mass and heat transport that influence solidification. The strong electromagnetic levitation fields exert a magnetic pressure on the liquid sample that leads to strong deviations from a sphere-like geometry, which is needed for measurements of surface tension and mass density. These limitations are overcome if the electromagnetic levitation technique is applied in reduced gravity. In the environment of space, the forces to compensate disturbing accelerations are some orders of magnitude smaller compared with experiments on ground. A special instrument called TEMPUS

(TEMPUS is a German acronym for Tiegelfreies Elektro-Magnetisches Prozessieren Unter Schwerelosigkeit.) has been designed to provide means of containerless processing in space [90].

A schematic view of the TEMPUS concept is shown in Figure 18. Positioning and heating is separated in TEMPUS by placing the sample into the superposition of a quadrupole and a dipole field of two independent coil systems. Both coil systems are powered independently by two rf generators at different radio frequencies. This two-coil concept has led to a drastic increase of the heating efficiency of an electromagnetically processed drop in reduced gravity compared to usual levitation on Earth. The coil system is integrated in a UHV chamber. The recipient can be backfilled with high purity Ar, He, and/or He-3.5%H_2 processing gas. Solidification of the undercooled melt can be externally triggered by touching the undercooled sample with a nucleation trigger needle, which is an integral part of the sample holder. The samples are transferred into the coil system from sample storage within ceramic cups or refractory metal cages.

Figure 18. Schematic view of the TEMPUS facility. All subsystems are shown with the exception of the radial temperature detector.

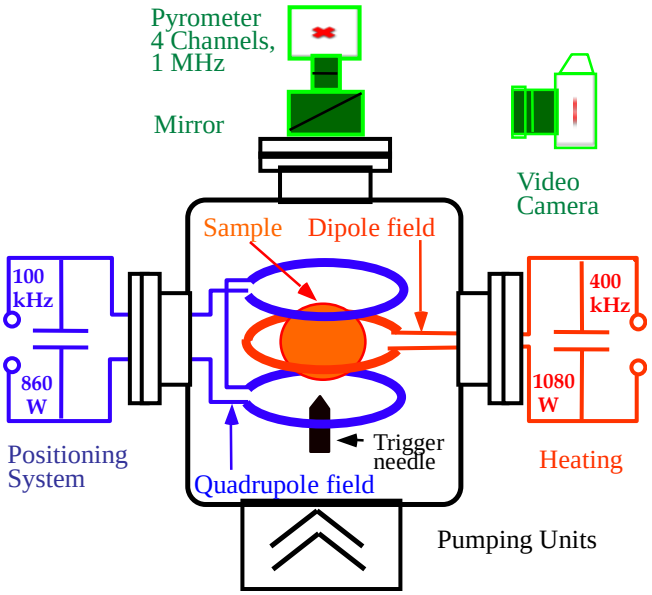

TEMPUS is equipped with pyrometers and video cameras. The sample is observed from two orthogonal views. From the top a pyrometer measures the temperature with a frequency of 1 kHz. A video camera is included in the optical path for sample observation with a maximum frame rate of 400 Hz. From the side, two different instruments can be installed, either a pyrometer specialized for measurements of the crystal growth velocity at rates up to 1 kHz (RAD), which is combined with a video camera with frame rates up to 400 Hz, or a high-resolution video camera (RMK) with special optics. The resolution is 10^{-4} for a 8 mm sample, as required for measurements of the thermal expansion. TEMPUS was successfully flown by NASA Spacelab missions IML2 (International Microgravity Laboratory 1994) and MSL1/MSL1R (Materials Science Laboratory 1997).

In a common effort by the DLR Space Agency and the ESA, an Electro-Magnetic Levitator (EML) is currently under development for use on board the International Space Station (ISS). It is under construction by ASTRIUM. Comparing with TEMPUS, some important improvements are realized. The first one concerns the coil design. While TEMPUS used two different coils, the EML facility will

make use of a new concept [91] such that only one coil system carries two different high frequency alternating currents. The first one operates at a frequency of 135–155 kHz, and serves as positioning system, whereas the second one operates at a frequency of 365–390 kHz and provides efficient heating. At maximum power, the positioning force in radial direction is about 80% and in axial direction about 120% of the force of the two-coil system of TEMPUS. The heating efficiency of EML is by a factor of 1.6 higher and the maximum heating power in the sample is about 30% higher compared with TEMPUS. The EML facility is equipped with axial temperature measurement and video observation of the sample. The temperature of the sample is measured by a one colour pyrometer in axial direction in the range between 573 K and 2373 K at an integration time of 5 ms and an accuracy better than 0.1 K at temperatures greater than 873 K and less than 3.0 mK in the temperature range 573 K–673 K. The measurement rate amounts to 100 Hz. An axial digital video camera allows to observing the sample during processing. The maximum resolution is 1280 × 1024 pixels, and the frame rate ranges between 15 Hz and 200 Hz, depending on the pixel density. In addition to the pyrometer and video system working in axial direction, a high-speed camera is used to observe the propagation of a rapidly moving solidification front. The maximum measuring frequency is 30 kHz at a sensor area of 256 × 256 pixels. In addition, thermal radiation monitoring from radial view is possible. At present, several international teams are preparing experiments to be performed in the EML facility on board the International Space Station, both to measure with high accuracy thermo-physical parameters of undercooled melts and studying physical mechanism of non-equilibrium solidification of undercooled melts [12].

4. Conclusions

Containerless processing by electromagnetic and electrostatic levitation has been applied to investigate crystal nucleation and rapid dendrite growth in undercooled melts of pure zirconium and pure nickel and various binary metallic alloys. Very large undercoolings were achieved. A statistical analysis of the distribution function of maximum undercoolings in electrostatic levitation experiments hints to the onset of homogeneous nucleation in undercooled Zr-melts. From the homogeneous nucleation rate calculated within classical nucleation theory, a lower limit of the solid-liquid interfacial energy was deduced. This value indicates that results by density functional theory and molecular dynamics simulations may lead to an underestimation of the solid-liquid interfacial energies. Comparative experiments on Earth, and in reduced gravity, of measurements of dendrite growth in undercooled $Al_{50}Ni_{50}$ clearly reveal the importance of forced convection on growth dynamics, which has to be taken into account to predict growth dynamics in undercooled melts in particular in the low undercooling range, in which the dendrite growth velocity is comparable, or even less than the fluid flow velocity in electromagnetically levitated melts. Non-equilibrium effects have been clearly detected by measurements of the dendrite growth velocity as a function of undercooling. In dilute $Ni_{99}Zr_1$ alloy a critical undercooling was identified at which a transition from chemically to pure thermally controlled growth is observed. As evidenced by neutron auto-radiography investigations on a similar dilute alloy, $Ni_{99}B_1$, it was demonstrated that this transition is accompanied by complete partitionless solidification leading to a metastable supersaturated solution. A similar phenomenon, disorder trapping was studied by undercooling experiments on the intermetallic compound $Al_{50}Ni_{50}$.

By measurements of the dendrite growth velocity of the equiatomic $Al_{50}Ni_{50}$ alloy at very large undercoolings, a transition from ordered to disordered growth of the B2 β-phase was identified. By taking into account a velocity dependent order parameter, dendrite growth theory was extended such that it describes quantitatively the dendrite growth velocity over the entire undercooling range accessible by containerless processing and reproducing the transition from ordered to disordered growth. This leads to the solidification of a metastable disordered superlattice structure of the intermetallic compound. Finally, a glass forming binary metallic alloy, $Cu_{50}Zr_{50}$, was investigated with respect to its dendritic growth dynamics. For the first time, a maximum in the dendrite growth velocity—undercooling relation was observed for a metallic alloy, which is a common feature for non-metallic glass forming systems. The analysis of these experiments reveal diffusion controlled growth in particular in the regime of temperatures between the maximum growth velocity and the glass transition temperature. All of these investigations prove containerless processing to be a powerful experimental tool to investigate phenomena of solidification, which are far away from equilibrium. They lead to various solid metastable materials. Hence, undercooling is an efficient parameter to control phase selection during solidification.

Acknowledgments

The author thanks all of his co-workers, in particular Peter Galenko, Jan Gegner, Dirk Holland-Moritz, Stefan Klein, Matthias Kolbe, Roman Lengsdorf, Thomas Volkmann and Haifeng Wang for their essential contributions to obtain the scientific results and for intense discussions. Thanks are to Florian Kargl for carefully proof reading the manuscript. Financial support by Deutsche Forschungsgemeinschaft within contracts HE1601/18, HE1601/21, HE1601/25, HE1601/26, DLR Space Agency within contract 50WM1140, and the European Space Agency within contract 15236/02/NL/SH is gratefully acknowledged.

Conflicts of Interest

The author declares no conflict of interest.

References

1. Herlach, D.M.; Cochrane, R.F.; Egry, I.; Fecht, H.-J.; Greer, A.L. Containerless processing in the study of metallic melts and their solidification. *Int. Mater. Rev.* **1993**, *6*, 273–347.
2. Herlach, D.M. Containerless undercooling and solidification of pure metals. *Annu. Rev. Mater. Sci.* **1991**, *21*, 23–44.
3. Rhim, W.-K.; Chung, S.K.; Barber, D.; Man, K.F.; Gutt, G.; Rulison, A.J.; Spjut, R.E. An electrostatic levitator for high temperature containerless materials processing in 1-g. *Rev. Sci. Instrum.* **1993**, *64*, 2961–2970.
4. Meister, T.; Werner, H.; Lohoefer, G.; Herlach, D.M.; Unbehauen, H. Gain-scheduled control of an electrostatic levitator. *Eng. Pract.* **2003**, *11*, 117–128.

5. Notthoff, C.; Franz, H.; Hanfland, M.; Herlach, D.M.; Holland-Moritz, D.; Petry, W. Energy-dispersive X-ray diffraction combined with electromagnetic levitation to study phase-selection in undercooled melts. *Rev. Sci. Instrum.* **2000**, *71*, 3791–3796.
6. Shuleshova, O.; Löser, W.; Holland-Moritz, D.; Herlach, D.M.; Eckert, J. Solidification and melting of high-temperature materials: *In situ* observations by synchrotron radiation. *J. Mater. Sci.* **2012**, *47*, 4497–4513.
7. Schenk, T.; Holland-Moritz, D.; Simonet, V.; Bellisent, R.; Herlach, D.M. Icosahedral short-range order in deeply undercooled metallic melts. *Phys. Rev. Lett.* **2002**, *89*, 075507. doi:10.1103/PhysRevLett.89.075507.
8. Kelton, K.F.; Lee, G.W.; Gangopadhyay, A.K.; Hyers, R.W.; Rathz, T.; Rogers, J.; Robinson, M.B.; Robinson, D. First X-Ray Scattering Studies on Electrostatically Levitated Metallic Liquids: Demonstrated Influence of Local Icosahedral Order on the Nucleation Barrier. *Phys. Rev. Lett.* **2003**, *90*, 195504:1–195504:5.
9. Kelton, K.F.; Greer, A.L.; Herlach, D.M.; Holland-Moritz, D. The Influence of Order on the Nucleation Barrier. *Mater. Res. Bull.* **2004**, *29*, 940–944.
10. Notthoff, C.; Feuerbacher, B.; Frans, H.; Herlach, D.M.; Holland-Moritz, D. Direct determination of metastable phase diagram by synchrotron radiation experiments on undercooled metallic melts. *Phys. Rev. Lett.* **2001**, *86*, 1038–1041.
11. Funke, O.; Phanikumar, G.; Galenko, P.K.; Chernova, L.; Reutzel, S.; Kolbe, M.; Herlach, D.M. Dendrite growth velocity in levitated undercooled nickel melts. *J. Cryst. Growth* **2006**, *297*, 211–222.
12. *Solidification of Containerless Undercooled Melts*; Herlach, D.M., Matson, D.M., Eds.; Wiley-VCH: Weinheim, Germany, 2012.
13. Skripov, V.P. *Material Science, Crystal Growth and Materials*; Pergamon Press: Amsterdam, The Netherlands, 1977.
14. Christian, J.W. *The Theory of Transformations in Metals and Alloys*; Pergamon: Oxford, UK, 1975.
15. Turnbull, D. Formation of Crystal Nuclei in Liquid Metals. *J. Appl. Phys.* **1950**, *21*, 1022–1028.
16. Nelson, D.R.; Spaepen, F. Polytetrahedral order in condensed matter. In *Solid State Physics*; Academic Press: New York, NY, USA, 1989.
17. Turnbull, D. Under what conditions can a glass be formed? *Contemp. Phys.* **1969**, *10*, 473–488.
18. Dantzig, J.A.; Rappaz, M. *Solidification*; EPFL Press: Lausanne, Switzerland, 2009.
19. Marr, D.W.; Gast, A.P. On the solid-fluid interface of adhesive spheres. *J. Chem. Phys.* **1993**, *99*, 2024–2030.
20. Sun, D.Y.; Asta, M.; Hoyt, J.J. Crystal-melt interfacial free energies and mobilities in fcc and bcc Fe. *Phys. Rev. B* **2004**, *69*, 174103:1–174103:9.
21. Klein, S.; Holland-Moritz, D.; Herlach, D.M. Crystal nucleation in undercooled liquid zirconium. *Phys. Rev. B (BR)* **2009**, *80*, 212202:1–212202:4.
22. Schleip, E.; Willnecker, R.; Herlach, D.M.; Görler, G.P. Measurements of ultra-rapid solidification rates in greatly undercooled bulk melts by a high speed photosensing device. *Mater. Sci. Eng. A* **1988**, *98*, 39–42.
23. Schleip, E.; Herlach, D.M.; Feuerbacher, B. External seeding of a metastable metallic phase. *Europhys. Lett.* **1990**, *11*, 751–756.

24. Cech, R.E. Evidence of solidification of a metastable phase in Fe-Ni alloys. *Transactions AIME* **1956**, *206*, 585–590.
25. Cech, R.E.; Turnbull, D. Heterogeneous nucleation of the martensitic transformation. *Transactions AIME* **1956**, *206*, 124–130.
26. Kim, Y.-W.; Lin, H.-W.; Kelly, T.F. Solidification structures in submicron spheres of iron-nickel: Experimental observations. *Acta Metall.* **1988**, *36*, 2525–2536.
27. Löser, W.; Garcia-Escorial, A.; Vinet, B. Metastable phase formation in eletromagnetic levitation, drop-tube and gas-atomization techniques: A comparative study. *Int. J. Non-Equilib. Process.* **1998**, *11*, 89–111.
28. Galenko, P.K.; Sobolev, S. Local non-equilibrium effect on undercooling in rapid solidification of alloys. *Phys. Rev. E* **1997**, *55*, 343. doi:10.1103/PhysRevE.55.343.
29. Galenko, P.K.; Danilov, D.A. Local non-equilibrium effect on rapid dendritic growth in binary alloy melt. *Phys. Lett.* A **1997**, *235*, 271–278.
30. Brener, E.; Melnikov, V.I. Pattern selection in two-dimensional dendrite growth. *Adv. Phys.* **1991**, *40*, 53–97.
31. Hoyt, J.J.; Asta, M.; Karma, A. Method for Computing the Anisotropy of the Solid-Liquid Interfacial Free Energy. *Phys. Rev. Lett.* **2001**, *86*, 5530–5533.
32. Wang, Q.; Wang, L.-M.; Ma, M.Z.; Binder, S.; Volkmann, T.; Herlach, D.M.; Wang, J.S.; Xue, Q.G.; Tian, Y.J.; Liu, R.P. Diffusion-controlled crystal growth in deeply undercooled $Zr_{50}Cu_{50}$ melt on approaching the glass transition. *Phys. Rev. B* **2011**, *83*, 014202:1–014202:5.
33. Galenko, P. Extended thermodynamical analysis of a motion of the solid-liquid interface in a rapidly solidifying alloy. *Phys. Rev. B* **2002**, *65*, 144103:1–144103:8.
34. Galenko, P.K. Solute trapping and diffusionless solidification in a binary system. *Phys. Rev. E* **2007**, *76*, 031606:1–031606:9.
35. Kerrache, A.; Horbach, J.; Binder, K. Molecular-dynamics computer simulation of crystal growth and melting in $Al_{50}Ni_{50}$. *Europhys. Lett.* **2008**, *81*, 58001:1–58001:6.
36. Alexandrov, D.V.; Galenko, P.K. Selection criterion of stable dendritic growth at arbitrary Péclet numbers with convection. *Phys. Rev. E* **2013**, *87*, 062403:1–062403:5.
37. Herlach, D.M.; Galenko, P.K. Rapid solidification: *In situ* diagnostics and theoretical modeling. *Mater. Sci. Eng. A* **2007**, *449–451*, 34–41.
38. Lee, J.; Matson, D.M.; Binder, S.; Kolbe, M.; Herlach, D.M.; Hyers, R.W. Magnetohydrodynamic Modeling and Experimental Validation of Convection Inside Electromagnetically Levitated Co-Cu Droplets. *Metall. Mater. Trans. B* **2013**, *44*, doi:10.1007/s11663-013-9995-5.
39. Bouissou, P.; Pelce, P. Effect of a forced flow on dendritic growth. *Phys. Rev. A* **1989**, *40*, 6673–6680.
40. Jeong, J.-H.; Goldenfeld, N.; Danzig, J.A. Phase field model for three-dimensional dendritic growth with fluid flow. *Phys. Rev. E* **2001**, *64*, 041602:1–041602:14.
41. Karma, A.; Rappel, W.-J. Phase-field method for computationally efficient modeling of solidification with arbitrary interface kinetics. *Phys. Rev. E* **1996**, *53*, 3017–3021.
42. Beckermann, C.; Diepers, H.-J.; Steinbach, I.; Karma, A.; Tong, X. Modeling Melt Convection in Phase-Field Simulations of Solidification. *J. Comput. Phys.* **1999**, *154*, 468–496.

43. Reutzel, S.; Hartmann, H.; Galenko, P.K.; Schneider, S.; Herlach, D.M. Change of the kinetics of solidification and microstructure formation induced by convection in the Ni–Al system. *Appl. Phys. Lett.* **2007**, *91*, 041913:1–041913:3.
44. Barth, M.; Wei, B.; Herlach, D.M. Crystal growth in undercooled melts of the intermetallic compounds FeSi and CoSi. *Phys. Rev. B* **1995**, *51*, 3422–3428.
45. Hyers, R.W. Fluid flow effects in levitated droplets. *Meas. Sci. Technol.* **2005**, *16*, 394–401.
46. Coriell, S.R.; Turnbull, D. Relative roles of heat transport and interface rearrangement rates in the rapid growth of crystals in undercooled melts. *Acta Metall.* **1982**, *30*, 2135–2139.
47. Hoyt, J.J.; Asta, M.; Haxhimali, T.; Karma, A.; Napolitano, R.E.; Trivedi, R.; Laird, B.B.; Morris, J.R. Crystal-Melt Interfacers and Solidification Morphologies in Metals and Alloys. *Mater. Res. Soc. Bull.* **2004**, *12*, 935–939.
48. Rozas, R.E.; Kuhn, P.; Horbach, J. Particle-Based Computer Simulation of Crystal Nucleation and Growth Kinetics in Undercooled Melts. In *Solidification of Containerless Undercooled Melts*; Herlach, D.M., Matson, D.M., Eds.; Wiley-VCH: Weinheim, Germany, 2012; pp. 381–401.
49. Eckler, K.; Herlach, D.M. Measurements of dendrite growth velocities in undercooled pure Ni-melts—Some new results. *Mater. Sci. Eng. A* **1994**, *178*, 159–162.
50. Volkmann, T.; Dendrite growth in undercooled nickel, unpublished results.
51. Willnecker, R.; Herlach, D.; Feuerbacher, B. Evidence of nonequilibrium processes in rapid solidification of undercooled metals. *Phys. Rev. Lett.* **1989**, *62*, 2707–2710.
52. Eckler, K.; Cochrane, R.F.; Herlach, D.M.; Feuerbacher, B.; Jurisch, M. Evidence for a transition from diffusion- to thermally-controlled solidification in metallic alloys. *Phys. Rev. B Brief Rep.* **1992**, *45*, 5019–5022.
53. Arnold, C.B.; Aziz, M.J.; Schwarz, M.; Herlach, D.M. Parameter-free test of alloy dendrite-growth theory. *Phys. Rev. B.* **1999**, *59*, 334–343.
54. Galenko, P.K.; Reutzel, S.; Herlach, D.M.; Danilov, D.; Nestler, B. Modelling of dendritic solidification in undercooled dilute NiZr1alloy. *Acta Mater.* **2007**, *55*, 6834–6842.
55. Boettinger, W.J.; Aziz, M.J. Theory for the trapping of disorder and solute in intermetallic phases by rapid solidification. *Acta Metall.* **1989**, *37*, 3379–3391.
56. Aziz, M.J.; Boettinger, W.J. On the transition from short-range diffusion-limited to collision-limited growth in alloy solidification. *Acta Metall. Mater.* **1994**, *42*, 527–537.
57. Gandham, P.; Biswas, K.; Funke, O.; Holland-Moritz, D.; Herlach, D.M.; Chattopadhyay, K. Solidification of undercooled peritectic Fe–Ge alloy. *Acta Mater.* **2005**, *53*, 3591–3600.
58. Assadi, H.; Reutzel, S.; Herlach, D.M. Kinetics of solidification of B2 intermetallic phase in the Ni–Al system. *Acta Mater.* **2006**, *54*, 2793–2800.
59. Sutton, M.; Yang, Y.S.; Mainville, J.; Jordan-Sweet, J.L.; Ludwig, K.F., Jr.; Stephenson, G.B. Observation of a Precursor during the Crystallization of Amorphous $NiZr_2$. *Phys. Rev. Lett.* **1989**, *62*, 288–291.
60. Greer, A.L.; Assadi, H. Rapid solidification of intermetallic compounds. *Mater. Sci. Eng. A* **1997**, *226–228*, 133–141.
61. Boettinger, W.J.; Bendersky, L.A.; Cline, J.; West, J.A.; Aziz, M.J. Disorder trapping in Ni_2TiAl. *Mater. Sci. Eng. A* **1991**, *133*, 592–595.

62. Huang, Y.; Aziz, M.J.; Hutchinson, J.W.; Evans, A.G.; Saha, R.; Nix, W.D. Comparison of mechanical properties of Ni_3Al thin films in disordered FCC and ordered $L1_2$ phases. *Acta Mater.* **2001**, *49*, 2853–2861.
63. Assadi, H.; Greer, A.L. The interfacial undercooling in solidification. *J. Cryst. Growth* **1997**, *172*, 249–258.
64. Hartmann, H.; Holland-Moritz, D.; Galenko, P.K.; Herlach, D.M. Evidence of the transition from ordered to disordered growth during rapid solidification of an intermetallic phase. *Europhys. Lett.* **2009**, *87*, 40007:1–40007:6.
65. Herlach, D.M.; Galenko, P.K.; Holland-Moritz, D. *Metastable Solids from Undercooled Melts*; Cahn, R., Ed.; Pergamon Materials Series; Elsevier: Oxford, UK, 2007; pp. 1–432.
66. Greet, R.J.; Magill, J.H. An Empirical Corresponding-States Relationship for Liquid Viscosity. *J. Phys. Chem.* **1967**, *71*, 1746–1756.
67. Magill, J.H.; Plazek, D.J. Physical Properties of Aromatic Hydrocarbons. II. Solidification Behavior of 1,3,5-Tri-α-Naphthylbenzene. *J. Chem. Phys.* **1967**, *46*, 3757–3769.
68. Fuss, T.; Ray, C.S.; Lesher, C.E.; Day, D.E. Stress development and relaxation during crystal growth in glass-forming liquids. *J. Non-Cryst. Solids* **2006**, *352*, 434–443.
69. Fokin, V.M.; Nascimento, M.L.F.; Zanotto, E.D. Correlation between maximum crystal growth rate and glass transition temperature of silicate glasses. *J. Non-Cryst. Solids* **2005**, *351*, 789–794.
70. Wang, W.H.; Lewandowski, J.J.; Greer, A.L. Understanding the glass-forming ability of $Cu_{50}Zr_{50}$ alloys in terms of a metastable eutectic. *J. Mater. Res.* **2005**, 20, 2307–2313.
71. Oh, S.H.; Kauffmann, Y.; Scheu, C.; Kaplan, W.D.; Rühle, M. Ordered Liquid Aluminum at the Interface with Sapphire. *Science* **2005**, *310*, 661–663.
72. Oh, S.H.; Chisholm, M.F.; Kauffmann, Y.; Kaplan, W.D.; Luo, W.; Rühle, M.; Scheu, C. Oscillatory Mass Transport in Vapor-Liquid-Solid Growth of Sapphire Nanowires. *Science* **2010**, *330*, 489–493.
73. Jackson, K.A. The Interface Kinetics of Crystal Growth Processes. *Interface Sci.* **2002**, *10*, 159–169.
74. Ediger, M.D.; Harrowell, P.; Yu, L. Crystal growth kinetics exhibit a fragility-dependent decoupling from viscosity. *J. Chem. Phys.* **2008**, *128*, 034709:1–034709:6.
75. Hoyt, J.J.; Asta, M. Atomistic computation of liquid diffusivity, solid-liquid interfacial free energy, and kinetic coefficient in Au and Ag. *Phys. Rev. B* **2002**, *65*, 214106:1–214106:11.
76. Ashkenazy, Y.; Averback, R.S. Kinetic stages in the crystallization of deeply undercooled body-centered-cubic and face-centered-cubic metals. *Acta Mater.* **2010**, *58*, 524–530.
77. Herlach, D.M. Containerless Undercooling of Drops and Droplets. In *Solidification of Containerless Undercooled Melts*; Herlach, D.M., Matson, D.M., Eds.; Wiley-VCH: Weinheim, Germany, 2012.
78. Brillo, J.; Pommrich, A.I.; Meyer, A. Relation between Self-Diffusion and Viscosity in Dense Liquids: New Experimental Results from Electrostatic Levitation. *Phys. Rev. Lett.* **2011**, *107*, 165902:1–165902:5.
79. Holland-Moritz, D.; Stüber, S.; Hartmann, H.; Unruh, T.; Meyer, A. Ni self-diffusion in Zr-Ni(-Al) melts. *J. Phys.: Conf. Ser.* **2009**, *144*, 012119:1–012119:4.
80. Tang, C.G.; Harrowell, P. Anomalously slow crystal growth of the glass-forming alloy CuZr. *Nat. Mater.* **2013**, *12*, 507–511.

81. Bragard, J.; Karma, A.; Lee, Y.H.; Plapp, M. Linking Phase-Field and Atomistic Simulations to Model Dendritic Solidification in Highly Undercooled Melts. *Interface Sci.* **2002**, *10*, 121–136.
82. Meyer, A.; Wuttke, J.; Petry, W.; Randl, O.G.; Schober, H. Slow Motion in a Metallic Liquid. *Phys. Rev. Lett.* **1998**, *80*, 4455–4457.
83. Faupel, F.; Frank, W.; Macht, M.P.; Mehrer, H.; Naundorf, V.; Rätzke, K.; Schober, H.R.; Sharma, S.K.; Teichler, H. Diffusion in metallic glasses and supercooled melts. *Rev. Mod. Phys.* **2003**, *75*, 237–280.
84. Rony, P.R. *The Electromagnetic Levitation of Metals*; Technical Report UCRL-11411; Lawrence Radiation Laboratory/University of California: Berkeley, CA, USA, 1964.
85. Earnshaw, S. On the nature of the molecular forces which regulate the constitution of the luminiferous ether. *Trans. Camb. Philos. Soc.* **1842**, *7*, 97–112.
86. Rulison, A.J.; Watkins, J.L.; Zambrano, B. Electrostaic containerless processing system. *Rev. Sci. Instrum.* **1997**, *68*, 2856.
87. Meister, T. Aufbau und Regelung eines elektrostatischen Positionierers. Ph.D. Thesis, Ruhr-University, Bochum, Germany, 2000.
88. Felici, N. Forces et charges de petits objets en contact avec une électrode affectée d'un champ électrique. *Revue Générale d'Electricité* **1966**, *75*, 1145–1160.
89. Kordel, T.; Holland-Moritz, D.; Yang, F.; Peters, J.; Unruh, T.; Hansen, T.; Meyer, A. Neutron scattering experiments on liquid droplets using electrostatic levitation. *Phys. Rev. B* **2011**, *83*, 104205:1–104205:7.
90. Piller, J.; Knauf, R.; Preu, P.; Lohöfer, G.; Herlach, D.M. Containerless positioning and inductive heating under micro-g conditions. In Proceedings of the 6th European Symposium on Materials Sciences under Microgravity, Bordeaux, France, 2–5 December 1986; ESA SP-256; pp. 437–444.
91. Lohöfer, G. *TEMPUS Space Station Vorentwicklung, SUPOS Spulenentwicklung*; German Patent 38 36239 (1991) and DLR Internal Report 333, 2001; p. 76.